ChemElectroChem

Research Article
doi.org/10.1002/celc.202400047

Chemistry Europe
European Chemical Societies Publishing

www.chemelectrochem.org

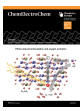

Photo-induced Intercalation of Cobalt(II) Tellurium Oxide as an Oxygen Evolution (Photo)electrocatalyst

Roelof J. Kriek,*[a] Oluwaseun A. Oyetade,[a] Nyengerai H. Zingwe,[a] Emanuela Carleschi,[b] Bryan P. Doyle,[b] and Jaco Koch[c]

Herein, we report on (a) the application of cobalt(II) tellurium oxide (Co_3TeO_6) as a photo-electrocatalyst, to enhance the photo-electrocatalytic (PEC) oxygen evolution reaction (OER) in alkaline media, compared to the electrocatalytic (EC) OER (in the absence of light), and (b) to store charge upon illumination and release charge upon the termination of illumination under OER potential bias conditions. These nanomaterials were synthesized employing the sol-gel method and calcined at temperatures ranging from 400 to 1100 °C. They were physically characterized and tested for their capacity to (i) act as a catalyst towards the OER, under EC and PEC conditions, and (ii) to convert and store light-energy as chemical-energy. Under PEC conditions CTO-900, which predominantly consisted of Co_3TeO_6, exhibited a five-fold increase in activity compared to EC conditions as current density increased from 0.58 mA cm^{-2} (EC) to 3.10 mA cm^{-2} (PEC) at 1.8 V (*vs.* RHE). Additionally, CTO-900 displayed the ability to not only store charge (upon illumination), but to also release this stored charge (after the termination of illumination), realising a current density of 2.07 mA cm^{-2} in the dark (under OER potential bias conditions). Photo-induced charge storage is due to the intercalation of potassium ions into Co_3TeO_6.

1. Introduction

Photo-electrocatalytic (PEC) water splitting has been recognised as a promising technique to provide clean and renewable energy. Since the pioneering work of Fujishima and Honda in 1972,[1] tremendous interest has been ignited amongst researchers to work towards applying solar energy to split water into molecular hydrogen and oxygen. With solar energy being an inexhaustible natural resource,[2] much effort is exerted to develop an appropriate photocatalyst to convert solar energy into chemical energy as a store (and source) of clean energy.[3] This technique presents an alternative, and potentially clean and sustainable approach, compared to the current use of fossil fuels, in producing hydrogen.[4–6]

Unlike electrocatalytic (EC) water splitting, which only requires a potential bias,[7] the PEC technique also requires irradiation by ultraviolet/visible light to produce photogenerated carriers on the surface of the photocatalyst.[8] Efforts to design effective photocatalysts, that split water efficiently under ultraviolet/visible light irradiation, continue to grow as practical water splitting efficiencies are still limited. An effective photocatalyst should (i) be stable at extreme potentials, (ii) have appropriate band gap and band edge positioning, such that the absorption of light results in effective reduction/oxidation at the photocatalyst surface, and (iii) exhibit reduced electron-hole recombination rates to ensure efficient charge transport.[2,9]

The oxygen evolution reaction (OER) is a relatively complex step in the overall water splitting process as it involves a multi-step four-electron transfer to evolve one mole of oxygen. The process is therefore slow and severely hampers the overall efficiency of water electrolysis in general.[6,7] Many novel electrocatalytic nanomaterials, such as transition metal oxides/hydroxides,[10–15] metal phosphides and/or phosphates,[16–18] perovskite oxides,[19,20] metal chalcogenides,[6,21] carbon nanomaterials,[6,22,23] amongst many others, have been synthesized in an effort to achieve efficient OER in both alkaline and acidic media. Increased EC performance of these materials, to obtain low(er) overpotentials for the OER, has intensified the probing of these materials as active catalysts towards PEC water splitting. For example, single-metal oxides, such as TiO_2, was first applied by Fujishima and Honda (1972) as a photocatalyst, to achieve the oxidation of water, *i.e.* oxygen evolution, at the TiO_2 anode, and hydrogen evolution at the cathode, without the application of an external voltage.[1] Subsequent to this, Hodes *et al.* (1976) reported the application of tungsten trioxide (WO_3) as a photoanode, with sulphuric acid as an electrolyte, to achieve oxygen evolution.[24] Haematite (Fe_2O_3)[25] and bismuth vanadate ($BiVO_4$) thin films[26] were also reported as an excellent light-harvesting photo-electrocatalyst, exhibiting remarkable stability for PEC water splitting. Recent studies have shown that metal doping of heterostructured nanomaterials further boosts

[a] *Prof. R. J. Kriek, Dr. O. A. Oyetade, Dr. N. H. Zingwe*
Electrochemistry for Energy & Environment Group, Research Focus Area: Chemical Resource Beneficiation (CRB), North-West University, Potchefstroom 2531, South Africa
+27 18 299 2345
E-mail: cobus.kriek@nwu.ac.za

[b] *Prof. E. Carleschi, Prof. B. P. Doyle*
Department of Physics, University of Johannesburg, P.O. Box 524, Auckland Park 2006, South Africa

[c] *Dr. J. Koch*
Unit for Environmental Sciences and Management, North-West University, Potchefstroom 2531, South Africa

Supporting information for this article is available on the WWW under https://doi.org/10.1002/celc.202400047

PEC activity. Examples of these materials include, amongst others, Au-decorated ZnO,[27] Ti- and Sn-doped α-Fe_2O_3,[28] *in situ* thermal oxidation of Fe films into α-Fe_2O_3,[4] and α-Fe_2O_3/Au/TiO_2[29] photoanodes. Additionally, Ding *et al.* reported that the introduction of electrocatalysts as cocatalysts, onto a photoanode, serves to reduce the activation energy of the photoelectrocatalytic process, thus, improving the PEC activity.[8] For instance, Ding *et al.*[30] and Zeng *et al.*[5] applied cobalt borate (CoB_i) and WO_3, respectively, as cocatalysts on $BiVO_4$ photoanodes to produce a photo-electrocatalyst with increased PEC activity and stability compared to the bare $BiVO_4$. Similarly, cobalt phosphate (Co–P_i) was deposited onto α-Fe_2O_3 by Zhong and Gamelin (2010), to fabricate a photocatalyst with increased OER performance in alkaline media.[28] In fact, the authors reported that compared to α-Fe_2O_3 photo-anodes, a 5-fold increase in the photocurrent density and O_2 evolution rate was observed at +1.0 V *vs.* RHE using the Co–P_i/α-Fe_2O_3 composite photo-anodes.[28] Despite increased scientific breakthrough in this field, these photo-electrocatalysts suffer from rapid electron-hole recombination, thereby limiting electron migration, resulting in low PEC activity towards the evolution of oxygen. It has to be mentioned that these reported photo-electrocatalysts were only active while maintaining irradiation. These photo-electrocatalysts immediately lose their activity once illumination is terminated, due to the recombination of the excited electrons (in the conduction band) and holes (in the valence band). To this end, it would be advantageous to design and fabricate photo-electrocatalysts that could be photocharged, thereby bringing about increased charge separation and prolonged activity, to facilitate PEC water splitting after the termination of solar irradiation, *i.e.* in the dark.

On the topic of sustained photocatalytic/photo-electrocatalytic activity, subsequent to light interruption, limited successes have been reported. For instance, a TiO_2–WO_3 composite was reported to exhibit continued anticorrosion and antibacterial activity after the termination of UV irradiation.[32] Similarly, during illumination, α-MoO_3 thin films were shown to store a fraction of the excited charge in its layered crystalline structure *via* alkali cation intercalation (Li^+, Na^+ and K^+),[33,34] which allowed the catalyst to discharge its stored charge/electrons and be utilized under dark conditions. It has furthermore been shown that α-MoO_3 was able to be recharged with successive illuminations, allowing it to behave as an alkali-ion battery.[33] Of late, our research group have identified binary-metal oxides, containing tellurates, as active compounds for retaining PEC activity for prolonged periods after light interruption, *i.e.* under dark conditions.[7,35]

Investigations into the use of dual photocatalyst systems were also conducted. For example, Shi *et al.* effectively utilized a CoO@MoS_2 photocatalyst for water splitting.[36] Their study showed that the rate of hydrogen produced, employing the dual or co-catalyst, was four times higher than the amount produced when only CoO was utilized, whilst also remaining stable for up to 72 hrs when the analysis was terminated. Likewise, CoO–Co_3O_4 systems were also utilized for photocatalytic water splitting by Morion *et al.* and Xiao *et al.*, yielding a higher hydrogen evolution rate of 276 $\mu mol\,g^{-1}\,h^{-1}$ and an oxygen production rate of 6.10 $mmol\,g^{-1}\,h^{-1}$, respectively.[37–38] Wang *et al.* employed a CoO/$BiVO_4$ dual photocatalyst for the degradation of tetracycline with the co-catalyst realising higher degradation relative to the pure composite compounds of CoO and $BiVO_4$, which was attributed to more effective separation of photogenerated charges.[39] Dual cobalt-based photocatalysts have also found use in hydrogen generation such as in the study conducted by Yang *et al.* utilizing a Co_3O_4-CoO-g-C_3N_4 system that produced a significantly high hydrogen evolution rate of 4050.60 $\mu mol\,g^{-1}\,h^{-1}$.[40] Other studies on cobalt-based dual photocatalysts, which were capable of functioning effectively due to improved charge separation, include studies on water splitting[41–44] and photocatalytic degradation of organic compounds.[45–48] With the aforementioned studies being a case in point, cobalt oxide-type nanomaterials have been reported to show good electrocatalytic performance towards the OER, in part due to their high surface area.[14,49] Sidhureddy *et al.* explored the electrochemical activity of 1D nanorod-, 2D nanosheet-, and 3D nanocube-shaped Co_3O_4 for the OER in alkaline medium.[14] The 2D nanosheets exhibited higher electrocatalytic activities compared to the 1D and 3D Co_3O_4. This was attributed to variations in their surface area and oxygen deficiencies, with activity being dependent on the size and shape of the nanomaterials.[14] Additionally, metal-doped Co_3O_4 was reported to exhibit enhanced OER activity compared to bare Co_3O_4 due to increased oxygen deficiencies resulting from disordered atomic arrangement and smaller charge transfer resistance.[49] Tellurium oxide (TeO_2) has furthermore been identified as a good dopant for metal oxides, due to its high refractive index, excellent optical properties, with good elastic behaviour and electrical conductivity.[35] Previous work by us, investigating the application of metal-tellurium oxides, such as europium(III) tellurium oxide[35] and nickel(II) tellurium oxide,[7] as photo-electrocatalysts, have shown these materials to achieve improved OER activity upon light irradiation and sustained PEC activity (in excess of 40 minutes) subsequent to the termination of UV/visible light. This study, to investigate a cobalt-based photo-electrocatalysts that has the potential of maintaining its photo-induced activity for prolonged periods after the termination of illumination, was motivated by the aforementioned results. Here we report on (i) the synthesis of cobalt(II) tellurium oxide, *via* the sol-gel synthesis route, (ii) the physical characterisation of the nanomaterials, and (iii) the electrocatalytic, photo-electrocatalytic, and photocharged (dark current) activity of these nanomaterials, towards the OER (as a model reaction) in alkaline medium. The scope of this investigation is on the oxygen evolution reaction and does not include photo-electrocatalytic watersplitting and to that regard the production of hydrogen and oxygen will not be quantified so as to determine the faradic efficiency.

Experimental

Materials and Chemicals

Cobalt(II) nitrate hexahydrate ($Co(NO_3)_2.6H_2O$, 98%) was purchased from Associated Chemical Enterprises (Johannesburg, South Africa). The procurement of telluric acid (H_6TeO_6, 98%) and Nafion (5 wt% in mixture of lower aliphatic alcohols and H_2O) was made from Sigma–Aldrich (New Germany, South Africa), while ammonia solution (32%), absolute ethanol, sodium hydroxide (NaOH, 99%), potassium hydroxide (KOH) and citric acid (99%) were obtained from Merck Chemical (Pty.) Ltd. (Gauteng, South Africa). Vulcan Carbon XC-72 was employed to prepare the electrocatalyst ink suspensions. Milli-Q water (18 $M\Omega cm^{-1}$) was employed in the preparation of solutions.

Synthesis of Photo-Electrocatalysts

Cobalt tellurium oxides were synthesized at different calcination temperatures by employing the *sol-gel* method.[7,10] In brief, H_6TeO_6 (0.1 $mol.dm^{-3}$) was added to 50 cm^3 of a 2:1 (v/v) ethanol-water mixture and stirred for 30 mins at 30 °C. An appropriate amount of $Co(NO_3)_2.6H_2O$ (0.2 $mol.dm^{-3}$) was added to this solution, followed by the addition of the chelating agent (0.6 $mol.dm^{-3}$ citric acid) to facilitate solution mixture at a molecular level. The solution was allowed to stir for another 30 mins after which a cross-linking agent (2.5 cm^3 ethylene glycol) was added to the mixture. The solution pH was adjusted with appropriate amount of ammonia solution until pH 11 was reached. Then, the solution was heated at 70 °C with constant stirring to obtain a gel, and subsequently oven-dried (Ecotherm, Labotech) at 120 °C overnight. The obtained powder was crushed, by using a pestle and mortar, and heated in a furnace (Carbolite ELF 11/14B) at 300 °C for 2 h. The powder obtained was crushed again and apportioned into four samples. These samples were sintered at 400 °C, 700 °C, 900 °C and 1100 °C for 5 h. The samples were collected, ground, labelled CTO-400, CTO-700, CTO-900 and CTO-1100 and kept in a desiccator for further analysis and use.

Preparation of Electrocatalyst and Photo-Electrocatalyst Inks

Preparation of Ink for Electrochemical Investigation

The electrocatalyst ink suspension was prepared as described earlier.[7] A weight ratio of 1:1 of the electrocatalysts and Vulcan carbon was weighed in 1.5 cm^3 of ethylene glycol and sonicated for 60 mins. Afterwards, 0.4 cm^3 of Nafion and 0.2 cm^3 of 0.1 $mol.dm^{-3}$ NaOH were added to the solution to lower the acidity of Nafion. The suspension was ultrasonicated for an additional 60 mins. A 10 μL aliquot of the ink suspension was cast onto the glassy carbon electrode (GCE) inserts employing a micropipette and dried overnight in a vacuum oven at 70 °C. The catalyst loading (*L*) on the GCE was calculated as 0.37 $mg.cm^{-2}$ using Equation 1.

$$Catalyst\ loading\ (L) = \frac{Mass\ of\ catalyst\ /\ mg}{0.196\ cm^2} \quad (1)$$

Preparation of Ink for Photo-Electrochemical Investigation

The catalyst ink for PEC measurements was prepared by dissolving 30 mg of the photo-electrocatalysts in 1 cm^3 of ethylene glycol and ultrasonicated for 60 min. Afterwards, 0.4 cm^3 of Nafion and 0.2 cm^3 of 0.1 $mol.dm^{-3}$ NaOH solution was added to the suspension and sonicated for an additional 60 mins. A 10 μL aliquot of the ink suspension was cast onto the glassy carbon electrode inserts (GCEs) with the aid of a micropipette and dried overnight in a vacuum oven at 70 °C. Prior to ink deposition, the GCEs, with a geometric surface area of 0.196 cm^2, were prepared by polishing them with a 0.05 μm alumina suspension (Allied High Tech. Products Inc.). Thereafter, the GCEs were cleaned sequentially in Milli-Q water, ethanol and isopropanol under ultrasonication for 20 mins each. The GCEs were dried by exposing them to a stream of nitrogen gas.

Physical Characterization

Micrographs were obtained from the FEI Quanta 250 field emission gun scanning electron microscope (SEM), operated at an accelerating voltage of 15 kV and fitted with an integrated EDS system (Oxford Inca Instruments). The structure and size of the photo-electrocatalysts were investigated on a JOEL 2100 high-resolution transmission electron microscope (HRTEM). X-ray diffraction analysis was conducted with a Panalytical X'Pert Pro utilizing Co–Kα ($\lambda =$ 1.7902 Å) radiation and a scan duration of 5 hours per sample. Noise reduction and background removal was then applied using a Savitzky–Golay smoothing filter and a polynomial background reduction filter. Phase identification, noise reduction and background removal were conducted using QualX software. Rietfeld refinement was then conducted on identified phases using Profex software with an anisotropic displacement for all identified phases in order to quantify phases. UV–Vis absorption measurements were conducted on a Specord S600 UV–Vis diode-array spectrophotometer (Analytik Jena). X-ray photoemission spectroscopy (XPS) measurements were performed to obtain information about the electronic structure of the photo-electrocatalysts. This was conducted on a SPECS PHOIBOS 150 hemispherical electron energy analyser and a SPECS XR 50 M monochromatized X-ray source equipped with an Al anode emitting X-ray photons of energy $h\nu =$ 1486.71 eV (Al–Kα). The overall energy resolution (analyser + photon source) was set to 0.8 eV for the wide survey scan spectra, and 0.55 eV for high-resolution O 1s, Te 3d and Co 2p core level spectra. Data were acquired at room temperature in an ultra-high vacuum (UHV) chamber with a base pressure of ~ 2×10^{-10} mbar. Powder samples were mounted on the sample holder using carbon tape. Surface charging was neutralised by means of a low-energy electron flood gun operating at an electron energy of 2.5 eV and an electron current of 20 μA.

Electrochemical and Photo-Electrochemical Characterization

The electrochemical (EC) and photo-electrochemical (PEC) characterization were performed on an in-house built three-electrode jacketed electrochemical cell, manufactured from polypropylene, with a quartz tube slot to fit the UV lamp.[7,35] The EC and PEC activities of the prepared catalysts were performed by using separate inks (see *2.3.1* and *2.3.2*), since the presence of carbon may prevent the absorption of light on the nanomaterials. The temperature was kept constant at 25 °C by employing a Julabo F12-ED thermostatically controlled circulation water-bath.

A platinum wire (Pine Research Instrumentation) and Hg/HgO (Bio-Logic Science Instruments) electrodes were employed as the counter and reference electrodes, respectively. A rotating-disk working electrode (RDE) setup (Pine Research Instrumentation) was employed for the electrocatalytic and photo-electrocatalytic measurements. The prepared GCE was inserted into the RDE and linear polarization (linear sweep voltammetry) curves of the samples were recorded by employing a VSP double-channel potentiostat (Bio-Logic Science Instruments). A Philips UVC germicidal lamp (TUV PL-S 9W/2P) emitting short-wave UV radiation, with a sharp and

dominant peak at 253.7 nm, was used as the light source. The photometric data of the UV lamp has been reported previously.[35] Electrocatalytic (EC) and photo-electrocatalytic (PEC) measurements were conducted in O_2-saturated 0.1 mol.dm^{-3} KOH at 25 °C at an RDE rotation speed of either 0 or 1600 rpm. The calibration of the Hg/HgO electrode *vs.* RHE (reversible hydrogen electrode) was conducted in a H_2-saturated 0.1 mol dm^{-3} KOH solution and was measured as −0.935 V *vs.* RHE. All potentials were *IR*-corrected by employing Equation 2,

$$E_{IR\ corrected} = E_{app} - IR \quad (2)$$

where I is the current, R is the ohmic resistance of the electrochemical cell, and E_{app} is the applied potential. A single point high frequency impedance measurement was used to measure the ohmic resistance of the electrochemical cell (R), which generated 43.12 Ω (CTO-400), 42.34 Ω (CTO-700), 40.62 Ω (CTO-900) and 44.22 Ω (CTO-1100) respectively, in 0.1 mol dm^{-3} KOH solution.

Employing the OER as a model experiment, the EC and PEC activity of the material was probed by means of series of linear sweep voltammetry (LSV) measurements, recorded in an alkaline medium (0.1 mol dm^{-3} KOH) at a scan rate of 10 mV.s^{-1}. Experiments were conducted from 0 to 1 V *vs.* Hg/HgO by rotating the RDE at either 0 or 1600 rpm. Electrochemical impedance spectroscopy (EIS) measurements were conducted in the frequency range of 100 mHz to 200 kHz with a sinusoidal AC potential perturbation of 10 mV at 0.6 V *vs.* Hg/HgO.

2. Results and Discussion

2.1. Physical Characterization

The surface morphology, shape, size and structure of the synthesized nanomaterials were examined employing SEM and TEM. The micrographs shown in Figure 1 represent SEM images of (a) CTO-400, (b) CTO-700, (c) CTO-900 and (d) CTO-1100, while Figure 2 shows the TEM images of (a) CTO-400, (b) CTO-700, (c) CTO-900 and (d) CTO-1100 at the same magnification. Particle sizes of the nanomaterials were estimated from the collected TEM micrographs employing the ImageJ 1.53e software. Most notable is the increase in the particle size of the nanomaterial as the sintering temperature is increased. The particle sizes of CTO-400, CTO-700, CTO-900 and CTO-1100 were calculated as 9.45 nm, 20.85 nm, 100.8 nm and 179.9 nm, respectively. The SEM images shows that CTO-400 and CTO-700 are composed of smaller-sized highly agglomerated nanoparticles which overlay on one another (Figures 1a–b). Similar observation was noticeable from the TEM images of CTO-400 and CTO-700, shown in Figures 2(a–b). An agglomeration of nanoparticles and mixture of different sizes and phases of nanomaterials were observed for these nanomaterials, as displayed in Figures 2(a–b). Further increase in sintering temperature from 900 °C to 1100 °C resulted in less agglomeration, but larger particle sizes. This explains the change in particle size, surface morphology and shape that were noticed at higher

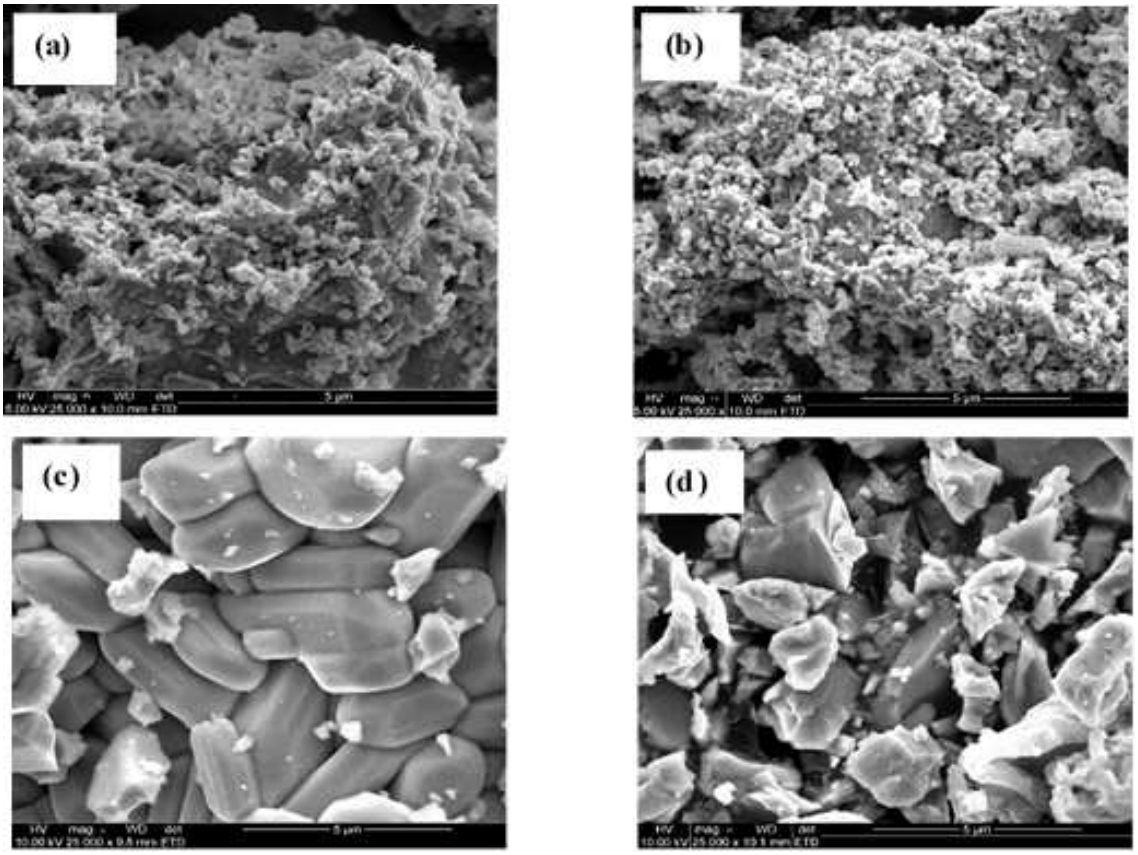

Figure 1. SEM images of (a) CTO-400, (b) CTO-700, (c) CTO-900, and (d) CTO-1100 at the same magnification.

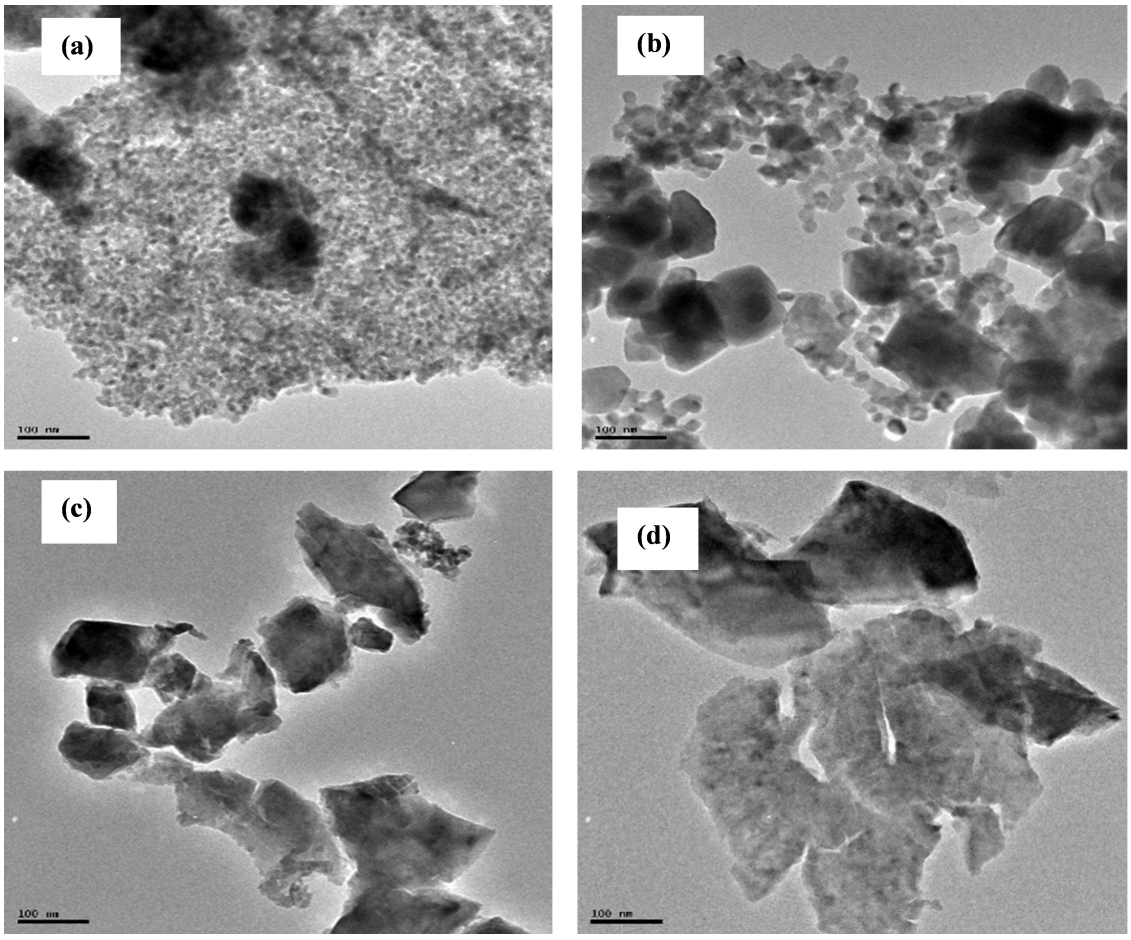

Figure 2. TEM images of (a) CTO-400, (b) CTO-700, (c) CTO-900, and (d) CTO-1100 at the same magnification.

calcination temperatures, *i.e.* 900 and 1100 °C, observed from Figures 1(c–d) and 2(c–d). Hexagonal-shaped particles were noticed at high temperatures, while the nanomaterials synthesized at lower sintering temperatures (400 and 700 °C) produced irregular spherical shaped nanomaterials (Figure 2). Our observations were compared with literature wherein nanomaterials were synthesized at varying calcination temperatures. Similar trends have been reported that also demonstrate larger particle sizes and distinct structures/phases at high sintering temperatures compared to nanomaterials obtained at lower temperatures.[7,35]

The compositional ratio of the synthesized nanomaterials was investigated by means of EDX analysis. The results presented in Table 1 provides the weight percentage of the different synthesized nanomaterials employed as (photo)electrocatalysts during linear sweep voltammetry experiments pre-illumination and post-illumination. The EDX data confirms the presence of constituent elements of Co, Te and O in the different nominal stoichiometric compositions. Tables 1 (weight%) and S2 (molar ratio) show that the composition of the CTO samples post experimental analysis remained relatively similar for all the CTO samples. This illustrates that the CTO samples remained stable after PEC and EC and do not degrade during analysis.

Table 1. EDX results (weight %) of cobalt (III) tellurium oxide samples employed as (photo)electrocatalysts during linear sweep voltammetry pre-illumination and post-illumination.

Samples	wt%, pre-illumination			wt.%, post-illumination		
	Co	Te	O	Co	Te	O
CTO-400	43.82	29.21	26.98	47.57	29.81	22.62
CTO-700	44.13	37.14	18.72	45.68	35.11	19.70
CTO-900	48.73	32.59	18.69	48.09	31.6	20.31
CTO-1100	53.93	23.62	22.44	52.45	24.52	24.03

The X-ray diffractograms of the synthesized nanomaterials, over the range $5^\circ \leq 2\theta \leq 100^\circ$, are presented in Figure 3. All the identified phases and peaks were matched to data obtained from the Crystallography Open Database (COD) sources listed in Table 2. All four temperature preparations display a dual phase compositional make-up with regards to the major components. CoO was identified as a major phase in all preparations which displayed an increasing trend with an increase in preparation temperature from 39.2 wt% at 400 °C to 48.9 wt% at 1100 °C. It is clear that CTO-400 exhibited no sharp and distinct peaks, which is due to the amorphous nature of the nanomaterial. An increase in the calcination temperature, however, serves to

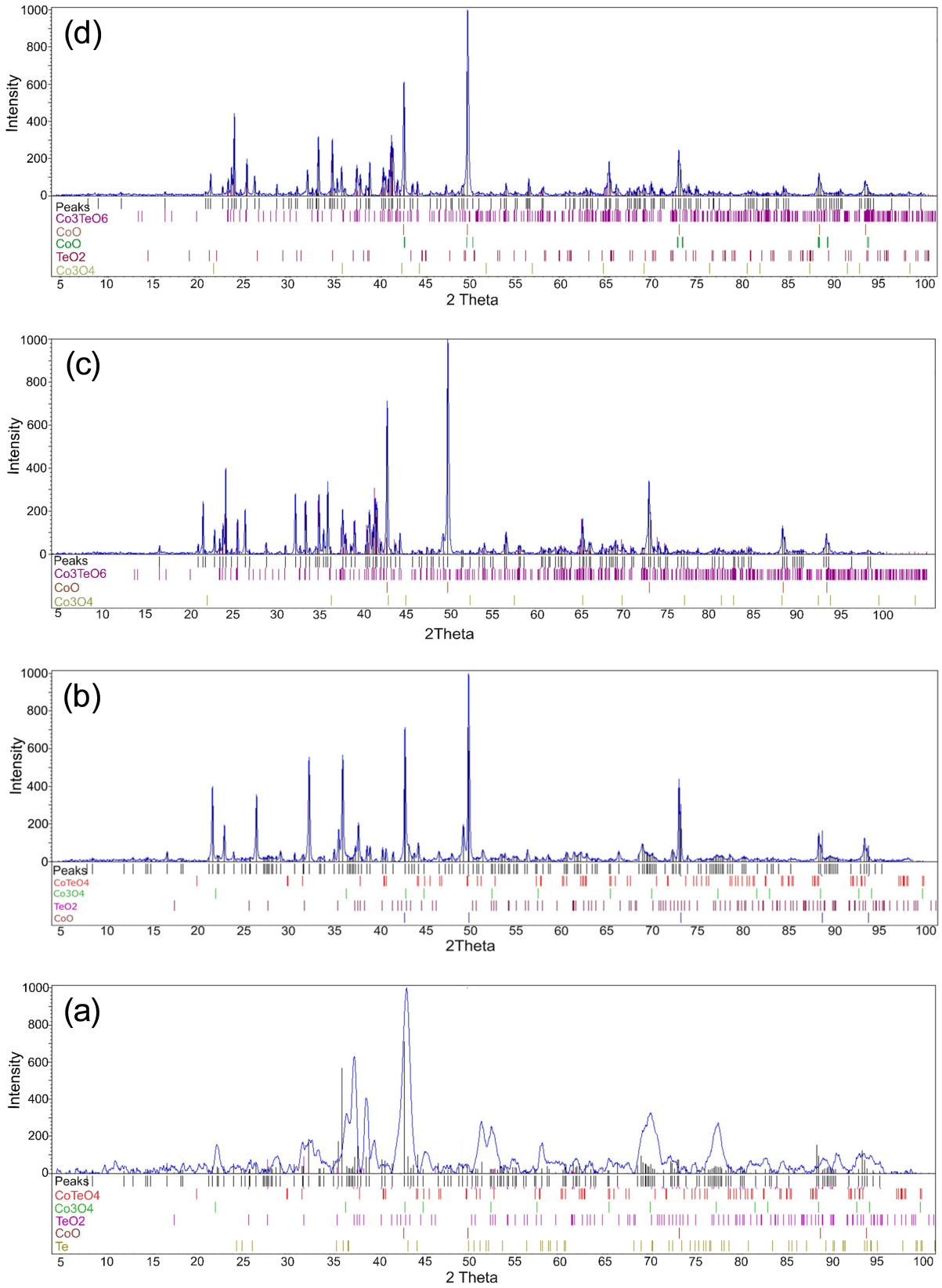

Figure 3. XRD diffractograms of cobalt(II) tellurium oxide nanomaterials at different calcination temperatures, i.e. (a) CTO-400, (b) CTO-700, (c) CTO-900, and (d) CTO-1100.

Table 2. COD (Crystallography Open Database) entry numbers and corresponding references.

Formula	COD	Reference
Te	00-153-3530	[50]
TeO_2	00-101-1183	[51]
Te_4O_9	00-210-6553	[52]
CoO	00-154-1642/00-154-1662	[53]
$CoTeO_4$	00-900-5890	[54]
Co_3O_4	00-900-5888/00-900-5890	[55,56]
Co_3TeO_6	00-201-5468	[57]

produce increasingly well-defined crystalline nanomaterials that exhibit more intense and sharp peaks. Temperatures of 400 °C and 700 °C also produced Co_3O_4 as a major phase, while temperatures of 900 °C and 1100 °C also produced Co_3TeO_6 as a major phase. A calcination temperature of 900 °C produced the greatest portion of Co_3TeO_6 at 54.8 wt%, compared to43.8 wt% at 1100 °C. At 400 °C unconverted Te was detected as a subordinate phase to CoO and Co_3O_4 at 16.1 wt%. This may indicate that 400 °C is ineffective in completely converting Te to the compounds of interest. Table 3 shows the weight percentages for the identified phases. Previous studies have also reported the formation of CoO nanoparticles at temperatures above 500 °C.[58] The presence of well-defined crystalline nanomaterials at 1100 °C, which include both CoO and Co_3TeO_6 phases, is proof to the fact that calcination temperature is an important parameter that determines phase formation and associated crystallinity.

XPS measurements were performed on all the nanomaterials. The wide survey spectra for the (photo)electrocatalysts are displayed in Figure 4. The core levels and Auger peaks have been labelled accordingly. C 1s was detected in all samples at a binding energy (BE) of ~285 eV. This was attributed to the presence of adsorbates on the surface of the samples, which is justified by the fact that all samples were prepared *ex-situ*. Shallow core levels below 50 eV BE are attributed to O 2s and Te 5s (not labelled in the figure). This valence band is the region closest to the Fermi energy. Comparison of the survey scans shows that there is a remarkable difference between CTO-1100 and the other three (photo)catalysts in terms of the intensity of the Te peaks, which is significantly reduced in CTO-1100. Below, we report evidence that the electronic structure of CTO-1100 shows further remarkable differences with respect to the other three catalysts.

The Te 3d core level spectra of the CTO samples are shown in Figure 5a. They are composed of two asymmetric peaks with centroids at ~576 eV and ~586.5 eV, which correspond to Te $3d_{5/2}$ and Te $3d_{3/2}$ spin-orbit components. Apart from CTO-1100, the asymmetry on the higher BE side confirms the presence of

Table 3. Results of XRD phase identification and quantification using Rietfeld refinement.

Temp (°C)	Identified Phases, Wt%						
	Te	TeO_2	Te_4O_9	CoO	Co_3O_4	$CoTeO_4$	Co_3TeO_6
400	16.1	5.5		39.2	35.4	3.8	
700		6.1		43.6	46.0	4.3	
900				43.5	1.6		54.8
1100			3.8	48.9	3.5		43.8

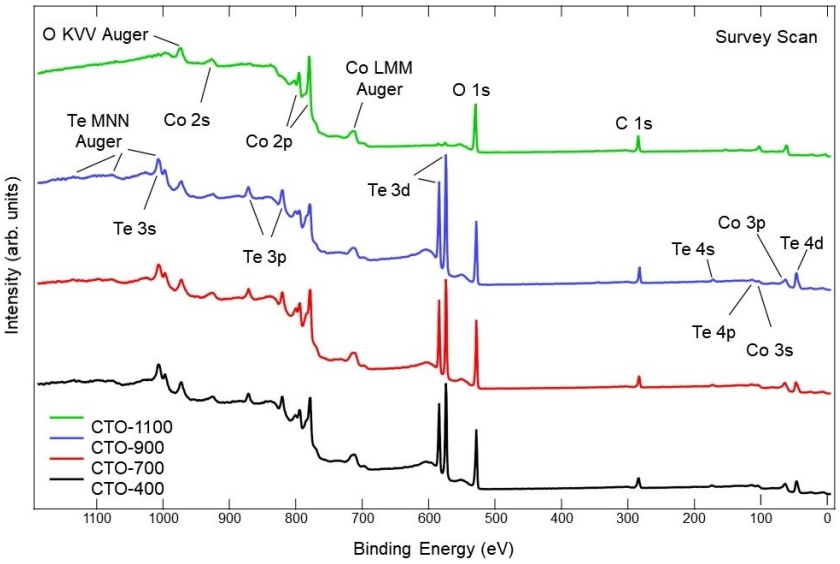

Figure 4. XPS wide survey scan of the CTO-400, CTO-700, CTO-900 and CTO-1100 photo-electrocatalyst samples.

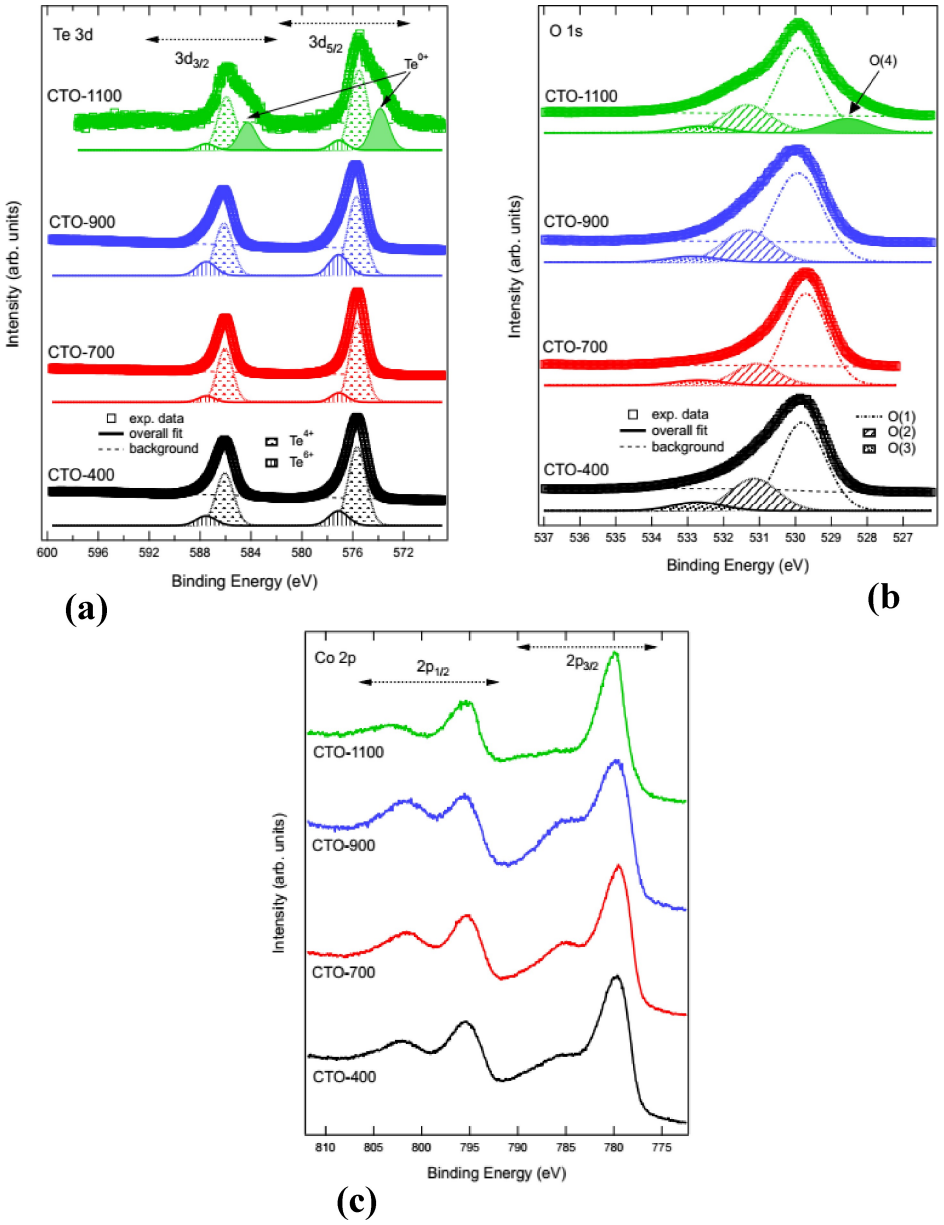

Figure 5. (a) Te 3d, (b) the O 1s and (c) the Co 2p core level spectra of CTO-400, CTO-700, CTO-900 and CTO-1100 photo-electrocatalyst samples.

two spin-orbit doublets that correspond to two different oxidation states for Te. The experimental data (open squares) was therefore fitted with two spin-orbit components, Te(1) and Te(2), and a Shirley-type background. The overall fit is plotted as a thick solid line on top of the data and shows very good agreement with it. The results of the fit are presented in Table 2. The BE of Te(1) and Te(2) are consistent with those reported for Te ions in +4 and +6 oxidation states, respectively.[7] We have therefore labelled them as Te^{4+} and Te^{6+} in the figure. These two oxidation states are typical of tellurium-based catalysts containing oxygen,[7,35] while those without oxygen Te tends to acquire +4 and +0 oxidation states.[59,60] For CTO-1100, the Te 3d core level spectrum is fundamentally different from the other three. Firstly, it is noisier because of the substantially lower Te XPS signal from this sample. Furthermore, there is a clear asymmetry on the lower BE side of the $3d_{5/2}$ and $3d_{3/2}$ main peaks, which was absent in the other three catalysts. This hints to the presence of an additional oxidation state for Te that is specific to this compound. The experimental data was fitted with three spin-orbit doublets and a Shirley background. The fit results reported in Table 4 show that two of these components have BEs that are consistent with those of CTO-400, CTO-700 and CTO-900 and correspond to Te^{4+} and Te^{6+} oxidation states. The additional one located at a lower BE is consistent with Te in a 0+ oxidation state and has therefore been labelled as Te^{0+} in Figure 5.[59,60] This additional Te^{0+} component takes up roughly one third of the spectral weight of the core level, causing the nominal valence of Te to decrease to 2.86 in this compound.

Although XPS and EDX are both spectroscopic techniques used in the identification of elements in a sample, it is

Table 4. BEs (in eV), FWHM (in eV) and relative percentage areas (in %) of the three components of the Te 3d core level.

Sample	Te^{0+} $3d_{5/2}$	Te^{4+} $3d_{5/2}$	Te^{6+} $3d_{5/2}$	Te^{0+} FWHM	Te^{4+} FWHM	Te^{6+} FWHM	Te^{0+} area	Te^{4+} area	Te^{6+} area	Nominal valence
CTO-400	N/A	575.66	577.14	N/A	1.66	1.81	N/A	83.2	16.8	4.34
CTO-700	N/A	575.65	577.10	N/A	1.46	1.51	N/A	89.5	10.5	4.21
CTO-900	N/A	575.73	577.12	N/A	1.64	1.79	N/A	77.5	22.5	4.45
CTO-1100	573.86	575.52	577.11	1.50	1.61	1.63	31.9	61.2	6.90	2.86

important to note that XPS is indeed a more surface-sensitive quantitative technique compared to EDX. The low amounts of Te demonstrated for CTO-1100 from the XPS analysis, as opposed to the EDX results presented in Table 1, could be attributed to (i) possible presence of Te in the less prominent phase (*i.e.* Co_3TeO_6) of CTO-1100, and/or (ii) the confinement of this phase in the bulk of the nanoparticles, and (iii) the formation of Co_3O_4 nanoparticles as a layer over the Co_3TeO_6 phase of the nanomaterial, which leads to the formation of a 'core-shell' type structure. We therefore hypothesize that low Te amounts in CTO-1100, shown by XPS peak intensities, could be attributed to either one or all of the aforementioned factors.

The O 1s core level spectra of the CTO catalysts are reported in Figure 5b. The raw data (open squares) overlaps very well with the overall fit (thick solid line). For CTO-400, CTO-700 and CTO-900, this was obtained by adding three single Voigt-type components and a Shirley-type background, with four singlets having been added together for CTO-1100. These components are labelled O(1), O(2), O(3) and O(4), and their BEs and other fitting parameters are presented in Table 5. The data interpretation was done according to relevant literature:[61,62] (i) the lower BE component O(1) is ascribed to the stoichiometric oxygen atoms in the main oxide lattice, (ii) O(2) is attributed to oxygen vacancies/defects in the lattice, and (iii) O(3) originates from chemisorbed contaminants on the sample surface. It should be noted that the spectra weight of O(3) is greater in CTO-900. It is important to note that O(4) is detected only in CTO-1100, and can be attributed to oxygen molecules bonded to either Te or Co.[63] The full-width-half-maximum (FWHM) of the four components is also reported in Table 3. The result illustrates that CTO-700 has the sharpest peaks (*i.e.* smaller FWHM). This observation is consistent with CTO-700 possessing the smallest percentage of oxygen vacancies. It is also interesting to note that the amount of oxygen vacancies ranges from roughly one third to one fourth with respect to that of the stoichiometric oxygen atoms, which is consistent with what has been observed in similar tellurium-based catalysts.[7,35,59]

Figure 5c reports the BE region of Co 2p core level spectra. The line shape of this core level is composed of two distinct regions: the Co $2p_{3/2}$ and Co $2p_{1/2}$ spin-orbit components. Each of these components features a main peak on the lower BE side and a corresponding satellite on the higher BE side. There are negligible differences in the line shape of this core level amongst CTO-400, CTO-700 and CTO-900 samples: the BEs of the main peaks and their 5.5 eV energy separation with their corresponding satellite are consistent with a majority $+2$ oxidation state for Co ions in these three CTO (photo)electrocatalysts.[64,65] CTO-1100 shows remarkable differences from the other three samples even in this core level: (i) the higher BE satellites appear very suppressed, (ii) the width of the main peaks is smaller and (iii) the line shape of the main peaks is more asymmetric towards the higher BE side. These features are consistent with the line shape of Co 2p displayed by Co_3O_4-type compounds, which hints at a $2+/3+$ mixed oxidation state for Co ions in this compound.[66] This finding is potentially consistent with the discussion on the XPS results related to the Te 3d core level of CTO-1100, where we hypothesise that Co_3O_4 nanoparticles are located more at the surface of this (photo)catalyst. This would indeed result in an increase in the spectral weight of their XPS signal in the Co 2p BE region, due to the intrinsic surface sensitivity of the XPS technique.

2.2. Electrochemical Characterization

The electrocatalytic activity of the synthesized nanomaterials, towards the OER in alkaline medium (as a model reaction), was investigated in the absence of any irradiation by employing linear sweep voltammetry (LSV). It was reported that a 1:1

Table 5. BEs (in eV), FWHM (in eV) and relative percentage areas (in %) of the four components of the O 1s core level.

Sample	O(1)	O(2)	O(3)	O(4)	O(1) FWHM	O(2) FWHM	O(3) FWHM	O(4) FWHM	O(1) area	O(2) area	O(3) area	O(4) area
CTO-400	529.81	531.15	532.72	N/A	1.51	1.56	1.7	N/A	67.4	25.3	7.3	N/A
CTO-700	529.71	531.09	532.68	N/A	1.41	1.45	1.6	N/A	76.5	18.6	4.9	N/A
CTO-900	529.93	531.34	532.87	N/A	1.64	1.6	1.62	N/A	70.6	24.8	4.6	N/A
CTO-1100	529.89	531.34	532.63	528.55	1.45	1.55	1.6	1.49	62.1	22	5.3	10.6

weight ratio of the electrocatalyst to Vulcan carbon exhibited the highest activity for tellurium oxide samples;[7] this ratio was also applied for the preparation of ink in this study. Figure 6 displays the OER activities (as LSV scans) of CTO samples calcined at different temperatures. At 1.8 V (*vs.* RHE), CTO-400 demonstrated the highest activity, followed by CTO-700, with the lowest electrocatalytic activity demonstrated by CTO-1100. This result demonstrates the effect that calcination temperature and crystallinity have on electrocatalytic activity. A similar trend was reported for europium(III) tellurium oxide, and for nickel(II) tellurium oxide, which also showed that the lowest electrocatalytic activity for OER in alkaline media (without any irradiation) was achieved for those samples with less amorphous character.[7,35] This behaviour could be associated with variations in the number of active surface sites, the intrinsic ability to adsorb hydroxy groups (OH^-), and differences in the electronic structure (electron mobility) of the electrocatalyst.[7,14]

The adsorption of OH^- ions onto the surface of the electrocatalyst results in the formation of intermediate species of M–OH, M–O, M–OOH, and M–OO through the bonded M–O, followed by the formation of an O–O bond.[6,7] The mechanism responsible for OER on metal-based surfaces is presented below (Reactions 3–7):[67–69]

$$M + OH^- \rightarrow M{-}OH^* + e^- \quad (3)$$

$$M{-}OH^* + OH^- \rightarrow M{-}O^* + H_2O + e^- \quad (4)$$

$$M{-}O^* + OH^- \rightarrow M{-}OOH^* + e^- \quad (5)$$

$$M{-}OOH^* + OH^- \rightarrow M{-}OO^* + H_20 + e^- \quad (6)$$

$$M{-}OO^* \rightarrow M + O_2 \quad (7)$$

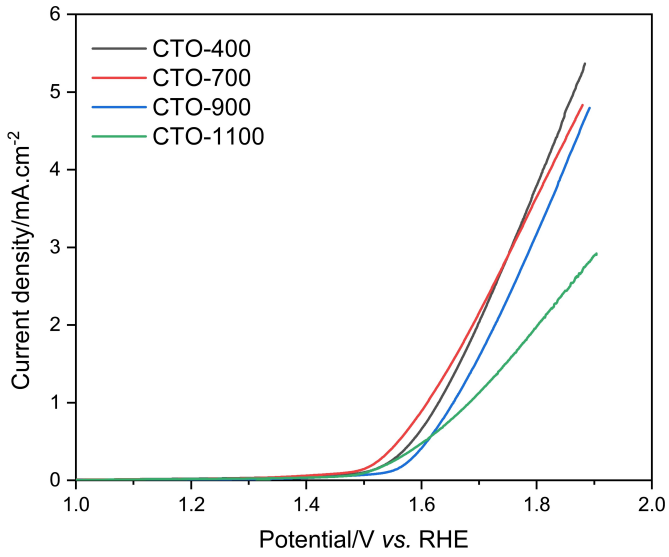

Figure 6. LSV curves for CTO samples (conditions: scan rate of 10 $mV.s^{-1}$, at 25 °C and 1600 rpm in oxygen-purged 0.1 $mol.dm^{-3}$ KOH electrolyte; in the absence of any irradiation).

An EIS analysis of the synthesized electrocatalysts was conducted to gain insight into the electrical resistance of the electrocatalyst-electrolyte interface. This was conducted within the OER region (0.6 V *vs.* Hg/HgO) and the associated Nyquist plots are presented in Figure 7a. The experimental EIS data were fitted with an equivalent circuit, by using the EIS Spectrum Analyser, employing parameters such as, the uncompensated solution resistance (R_s), charge transfer resistance (R_{ct}), charge transfer rate constant (k_{ct}), and double-layer capacitance (C_1), presented in Table S1. A semi-circular arc was obtained for each electrocatalyst (Figure 7a), demonstrating their charge transfer resistance (Figure 7a and b). It was observed that the CTO-400 demonstrated the lowest charge transfer resistance, followed by CTO-700, CTO-900, and CTO-1100, respectively (Table S1). Most notably, the electrocatalytic activity ($i/mA\,cm^{-2}$) of these electrocatalysts towards the OER (Figure 6, at 1.8 V *vs.* RHE) was observed to follow a similar trend as that of the charge transfer rate constant, k_{ct}, and an inverse trend to that of the charge transfer resistance, R_{ct} (Figure 7b). The higher the R_{ct}-value of an electrocatalyst, the lower its electrocatalytic activity towards the OER. Thus, CTO-400 demonstrated better electrocatalytic performance towards the OER compared to its counterparts, due to its increased charge transfer ability, i.e. electron mobility.

In order to further evaluate the OER capabilities of the developed CTO samples, analysis of the electrochemical surface area (ECSA) data obtained through the double layer capacitance

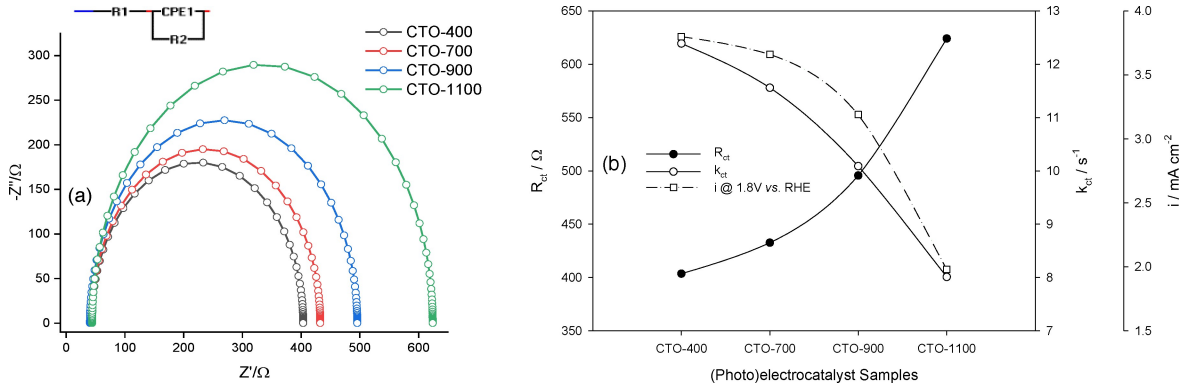

Figure 7. (a) EIS spectra, and (b) charge transfer values (R_{ct} and k_{ct}) and OER current (i) for CTO samples (conditions: oxygen-purged 0.1 $mol.dm^{-3}$ KOH electrolyte; in the absence of any irradiation).

method was conducted. Since the double layer capacitance is linearly proportional to the ECSA through the equation ECSA = C_{dl}/C_s thus its analysis gives insight into the catalytic performance of the CTO samples. Figure S4 shows the linear relationship from cyclic voltammetry results, between the current density and scan rate that was utilized to calculate the double layer capacitance. The C_{dl} for the CTO samples were determined to be 4.34, 3.03, 5.1 and 2.95 $mF \cdot cm^{-2}$ for CTO-400, CTO-700, CTO-900 and CTO-1100 respectively. As a result, the CTO-900 sample possessed the largest ECSA which yielded greater exposure for more catalytically active sites for the oxygen evolution reaction.

2.3. Photo-Electrochemical Measurements

Prior to PEC measurements, the UV–Vis absorption spectra of the synthesized nanomaterials were recorded. Figures S1a shows the absorption spectra for CTO-400 and CTO-900, respectively, with the most prominent peak at ~375 nm, with a red shift observed for CTO-900 calcined at higher temperature. The occurrence of a small peak at ~460 nm was also noticeable for CTO-900 (at the higher calcination temperature). The two peaks at 375 nm and 460 nm were attributed to the charge transfers O2p to Te5p and O2p to Co3d.[70–73] The optical band gap (E_g) of each of the nanomaterials was estimated from the Tauc plots (Figure S1b), according to Equation 8:

$$(\alpha h\upsilon)^2 = A\left(h\upsilon - E_g\right) \tag{8}$$

where E_g is the optical band gap, $h\upsilon$ is the photonic energy, α is the absorption coefficient, and A is the proportionality constant for the material. From the data, the optical band gaps (in eV) of the prepared oxides were determined to be 3.18, 3.15, 3.10 and 3.04 for CTO-400, CTO-700, CTO-900 and CTO-1100 respectively, thereby, demonstrating that all the nanomaterials are UV-light active, hence, the choice of lamp employed in the PEC study that emits at 253.7 nm. The bandgaps were obtained through extrapolating the linear part of the $(F(R).hv)^2$ curve such that it intercepts with the x (hv) axis as shown in Figure S1b. The decrease in bandgap as the calcination temperature increases for the CTO samples from 3.18 eV for CTO-400 to 3.04 eV for CTO-1100 is due to an increase in the amplitude of atomic vibrations, which results in a significantly larger interatomic distance. Resultantly a reduction in the energy bandgap occurs from the reduction in periodic potential caused by the increase in the interatomic spacing. Further studies into the wavelength dependent photoelectrochemical capabilities of the CTO samples were conducted through analysis of incident photon conversion efficiency (IPCE) measurements for CTO-900 as shown in Figure S1c. The CTO-900 sample curve reached a maximum of 22% at 387 nm. The reduction in IPCE from the peak towards higher wavelength was attributed to the effect of d-d transitions, which primarily dominate the optical absorption spectra at higher wavelength and results in localized excitations. This modest IPCE value obtained in the current study suggest that bulk recombination reactions, which largely affect photogenerated charges, were limited to some extent.

The photo-electrocatalytic (PEC) activities of the synthesized nanomaterials, towards the OER, were investigated in the absence of Vulcan carbon and estimated from LSV curves obtained at a scan rate of 10 $mV.s^{-1}$. Current density-potential curves (LSVs) at 0 rpm (Figure S2) and 1600 rpm (Figure 8), in oxygen-purged 0.1 $mol.dm^{-3}$ KOH solution with variable illumination times (0–150 min) clearly depict an increase in activity from EC to PEC with the greatest activity increase being observed for the CTO-900 sample. This is clearly evident when plotting the current densities, at 1.8 V (*vs.* RHE), for each (photo)electrocatalyst at different illumination times (see Figure 9). In the absence of forced mass transfer (Figure 9a), the PEC activity declined in the order CTO-900 > CTO-700 > CTO-1100 > CTO-400, while under forced mass transfer conditions (Figure 9b), the PEC activity declined in the order CTO-900 > CTO-1100 > CTO-700 ≈ CTO-400.

A general observation would infer that the EC activity is more positively affected by the amorphous nature and surface properties of the sample(s) calcined at lower temperatures, while the PEC activity is more positively affected by the increased crystalline nature of the samples calcined at higher temperatures. Our results agree with previously published data that also reports improved PEC activity for nanomaterials calcined at higher temperatures.[7,35] It is, however, observed that the CTO-1100 sample exhibited lower PEC activity compared to the CTO-900 sample, at both 0 and 1600 rpm. This could be attributed to mixed phases being present in the CTO-1100 sample that would seem to exhibit a 'core-shell type' structure, with the shell consisting of Co_3O_4 while the core consists of Co_3TeO_6, as inferred by the XPS data. The CTO-900 sample, consisting predominantly of Co_3TeO_6, does not have this Co_3O_4 outer layer (that would seem to inhibit PEC activity) and to that regard exhibits superior activity compared to CTO-1100.

The CTO-900 compares favourably to previously reported photo-electrocatalysts applied for the OER in alkaline medium (Table 6). For instance, at the same potential, *i.e.* 1.8 V (*vs.* RHE), nitrogen-doped ZnO nanowire only exhibited a photocurrent density lower than 0.3 $mA.cm^{-2}$, compared to CTO-900 that

Table 6. Comparison of the PEC current densities of previously synthesized nanomaterials.

Photo-electrocatalyst	Current density/$mA.cm^{-2}$ (at 1.8 V *vs.* RHE)	Ref.
Eu_2TeO_6	2.66	[35]
$NiTe_2O_5$	3.60	[7]
$Eu_2O_3/BiVO_4$	< 0.15	[75]
$BiVO_4$	< 0.12	[75]
Pure TiO_2	0.86	[75]
TiO_2 nanotubes	< 0.2	[74]
ZnO@TiO_2 core shell	< 0.7	[74]
ZnO nanowires	< 0.5	[74]
Co_3TeO_6	3.10	This Study

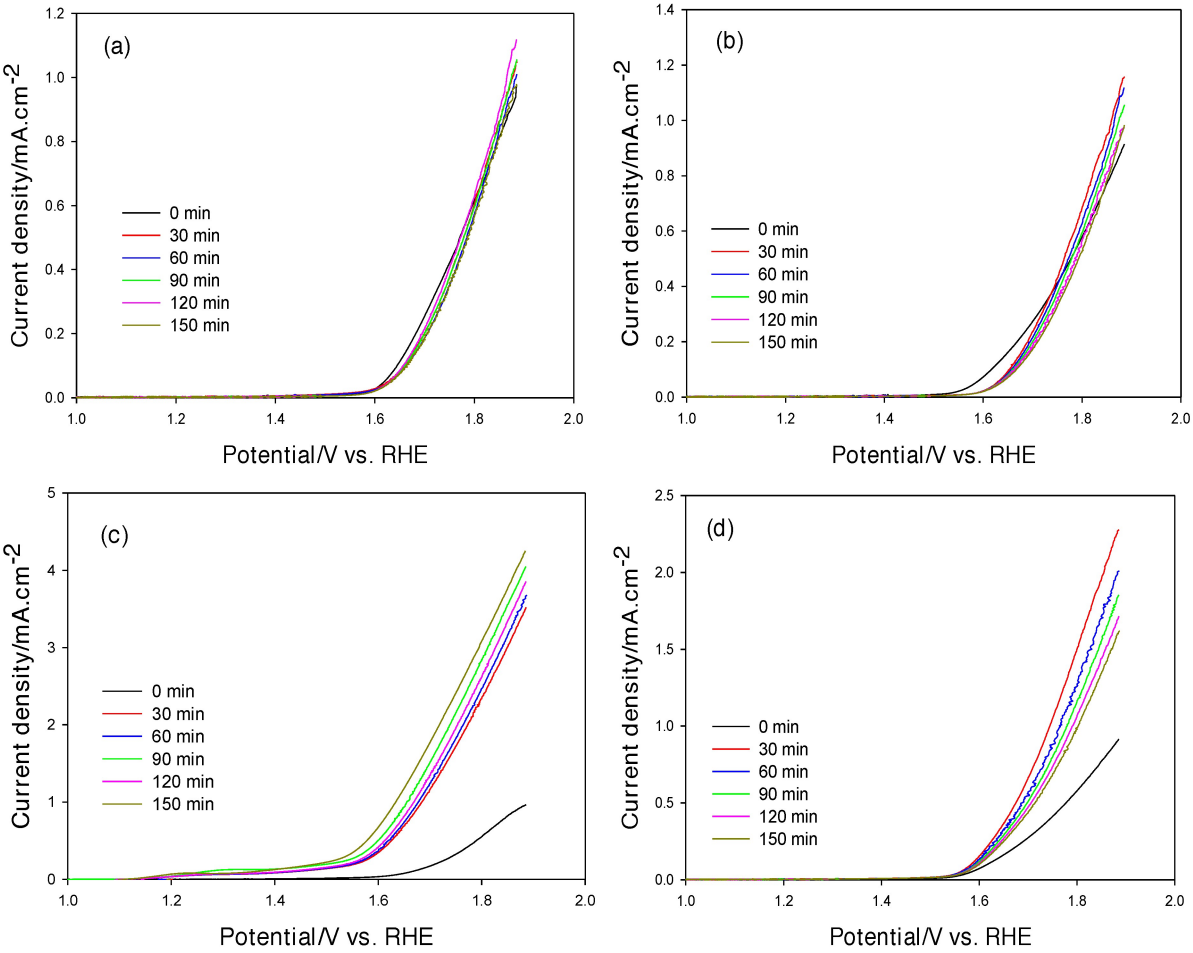

Figure 8. Current density-potential curves of (a) CTO-400, (b) CTO-700, (c) CTO-900 and (d) CTO-1100 for different illumination times (conditions: a scan rate of 10 mV.s^{-1}, at 25 °C and 1600 rpm in oxygen-purged 0.1 mol.dm^{-3} KOH electrolyte, under UV irradiation).

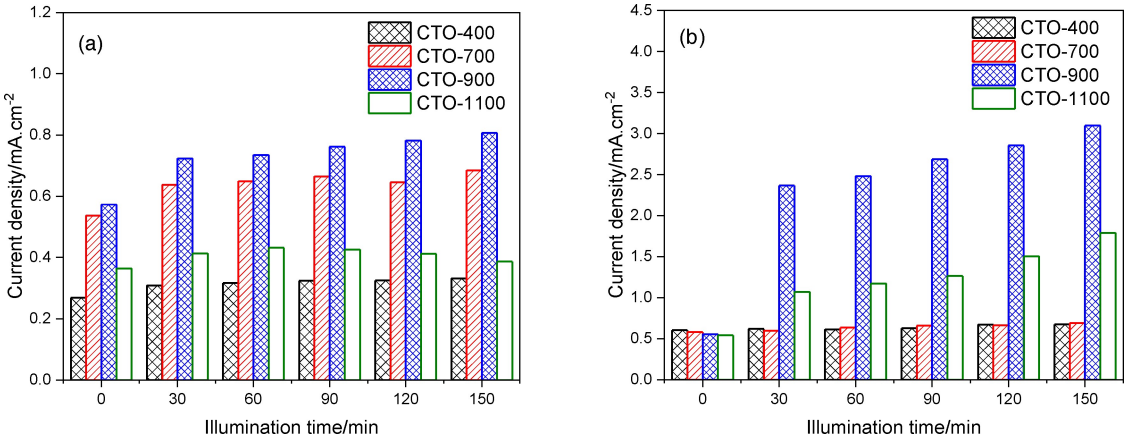

Figure 9. Current density *vs.* illumination time plots for CTO-400, CTO-700, CTO-900 and CTO-1100, at 1.8 V *vs.* RHE, for (a) 0 rpm, and (b) 1600 rpm, in oxygen-purged 0.1 mol.dm^{-3} KOH electrolyte at 25 °C.

produced a current density of 3.10 mA.cm^{-2}.[74] It is furthermore worthy to note that the PEC activity of CTO-900, after 30 min illumination time, was almost five times greater than its EC activity of 0.58 mA.cm^{-2} (at 1.8 V *vs.* RHE). In fact, an increase of greater than five times was observed for the nanomaterial after 150 min illumination time (Figure 9b). This can be ascribed to effective charge separation, *i.e.* the production of electron hole pairs, with the additional hole concentration, working together with the applied potential, contributing to an increased rate of

the OER. This result demonstrates the potential of CTO-900 as a photo-electrocatalyst for the OER in alkaline media.

To provide additional insight into the electronic behaviour of the best performing photo-electrocatalyst, electrochemical impedance spectroscopy (EIS) was conducted on CTO-900 at varying illumination times. The Nyquist plots for the photo-electrocatalyst, at different illumination times, exhibit a semi-circular arc that fits the *R-Q* equivalent circuit (Figure 10a). The circuit consist of a series resistance (R_s), a charge transfer resistance (R_{ct}), and a constant phase element (*CPE*). The *CPE*, also denoted as *Q*, is usually applied for real electrochemical systems, instead of a pure capacitor. This is due to different non-ideal parameters, such as roughness, porosity, and heterogeneity, at the catalyst surface, which may result in the production of frequency dispersion because of non-uniform distribution of the current density. In this study, the value of the *CPE* was kept constant throughout the experiment as a constant potential was applied throughout. The fitted parameters obtained for CTO-900 at varying time intervals, relating to the R–Q equivalent circuit, is presented in Table 7. A decrease in the R_{ct}-values is observed as the illumination time is increased; in fact, a two-fold decrease was obtained after 150 min of illumination, compared to the EC sample. This demonstrates the increased ability of the photo-electrocatalyst, with increased illumination time, to effectively separate the photo-induced electron-hole pairs, and therefore reduce the rate of their recombination. This results in enhanced charge separation, as well as migration of the photogenerated electron-hole pairs to the surface of the photo-electrocatalyst, which in turn results in an improved PEC water oxidation rate. The time constant (τ) and the charge transfer rate constant (k_{ct}) are calculated from Equations 9 and 10, respectively.

$$\tau = R_{ct}.Q \tag{9}$$

$$k_{ct} = \tau^{-1} \tag{10}$$

Of significant importance is to note that an increase in the illumination time resulted in an increase in the k_{ct}-values and a decrease in the τ-values (Table 7). Similarly, lower R_{ct}- and τ-values were obtained after 150 mins of light illumination, which suggest a slower recombination rate and reveals the ability of CTO-900 for increased PEC oxygen evolution at the anode with increasing illumination time.

A plot of R_{ct}- and k_{ct}-values as a function of illumination time depicts an exponential decrease in the charge transfer resistance, R_{ct}, together with an associated linear increase in the charge transfer rate constant, k_{ct} (Figure 10b). This is attributed to the increase in the charge carrier density observed with increased illumination time, resulting in an improvement in the overall energy conversion efficiency.

In line with our previous work on photo-induced charge storage and the subsequent discharge of the material in the dark (to bring about dark current OER), we investigated whether or not the CTO photo-electrocatalysts would exhibit similar behaviour. LSV curves were recorded (i) in the absence of any initial illumination, *i.e.* under an EC condition, (ii) under a PEC condition after 150 min of illumination, and (iii) under an EC condition, in the dark (from 10–40 min, with 10 min intervals), subsequent to a 150 min illumination time, at 0 rpm (Figure S3) and 1600 rpm (Figure 11). At 0 rpm the PEC current densities (at 1.8 V *vs.* RHE) do not exhibit much of an increase compared to the EC current densities (Figure 12a), however, at 1600 rpm a marked increase in the PEC current density is observed for the CTO-900 sample (in excess of a five-fold increase) and less so for the CTO-1100 sample (Figure 12b). At 1600 rpm, an active OER dark current is observed for the CTO-900 sample that is 73% of the 150 min PEC-value after 10 min in the dark. This decreased to 67% of the 150 min PEC-value after 40 min in the dark; at which point it still is almost a four-fold increase compared to the non-illuminated EC current (Figure 12b).

The observed phenomenon of charge/energy storage, resulting in an enhanced PEC current after 150 min of illumination, and an enhanced EC current after the termination of illumination, can be clarified through reactions 11–16. In the absence of light, under pure electrocatalytic (EC) conditions, the application of a positive potential bias (+PB) on the anode drives the oxygen evolution reaction (OER, reaction 11) on the

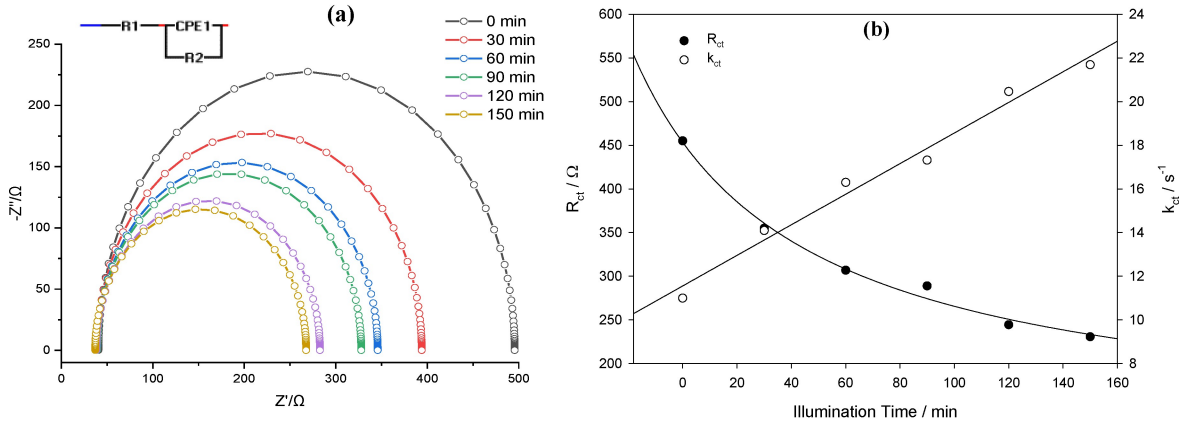

Figure 10. (a) EIS spectra of CTO-900 at varying illumination times in an O_2-purged 0.1 mol.dm^{-3} KOH electrolyte, and (b) plots of R_{ct} and k_{ct} for CTO-900 as a function of illumination time.

Table 7. Fitting parameters of the equivalent circuit element for CTO-900.

Sample	R_s/Ω	$Q/$ mF.s$^{(n-1)}$)	R_{ct}/Ω	n	τ/s	$k_{ct}/$ s^{-1}
EC	40.62	0.20	455.08	1	0.091	10.99
Light, PEC 30	39.22	0.20	354.80	1	0.071	14.09
Light, PEC 60	39.22	0.20	306.70	1	0.061	16.30
Light, PEC 90	39.16	0.20	288.74	1	0.058	17.32
Light, PEC 120	38.42	0.20	244.33	1	0.049	20.46
Light, PEC 150	37.16	0.20	230.54	1	0.046	21.69

surface of the CTO electrocatalyst generating an oxidative current.

$$Co_3TeO_6(+PB) + 4OH^- \rightarrow Co_3TeO_6(+PB) + O_2 + 2H_2O + 4e^- \quad (11)$$

In the presence of light and an applied potential bias, that is under PEC conditions, the regular CTO surface OER is driven (as per reaction 11) with illumination of CTO resulting in charge separation (reaction 12). The generated positive holes contribute in driving the OER (reaction 13) while the excited electrons are stabilised by the intercalation of the electrolyte cation (K^+, potassium ions) into the CTO layered structure (resulting in the formation of $K_4Co_3TeO_6$), which is deemed *(photo)charging* (reaction 13). Kanyolo *et al.*,[76] reported that metal tellurium oxides lend themselves to intercalation as they are layered structures. The nett reaction of the combination of reactions 12, 13 and 14 is portrayed in reaction 15.

$$Co_3TeO_6(+PB) \xrightarrow{h\nu} Co_3TeO_6(+PB;\ 4h^+ + 4e^-) \quad (12)$$

$$Co_3TeO_6(+PB;\ 4h^+ + 4e^-) + 4OH^- \rightarrow Co_3TeO_6(+PB;\ 4e^-) + O_2 + 2H_2O \quad (13)$$

$$Co_3TeO_6(+PB;\ 4e^-) + 4\,K^+ \rightarrow K_4Co_3TeO_6(+PB) \quad (14)$$

$$Co_3TeO_6(+PB) \xrightarrow[4KOH]{h\nu} K_4Co_3TeO_6(+PB) + O_2 + 2H_2O + 4\,h^0 \quad (15)$$

From the balanced reactions above (reactions 12–15) it would seem that photo-induced charge separation (reaction 12), the photo-induced OER (reaction 13), and photo-induced intercalation (reaction 14) all occur at the same rate (especially considering overall reaction 15). This, however, is an

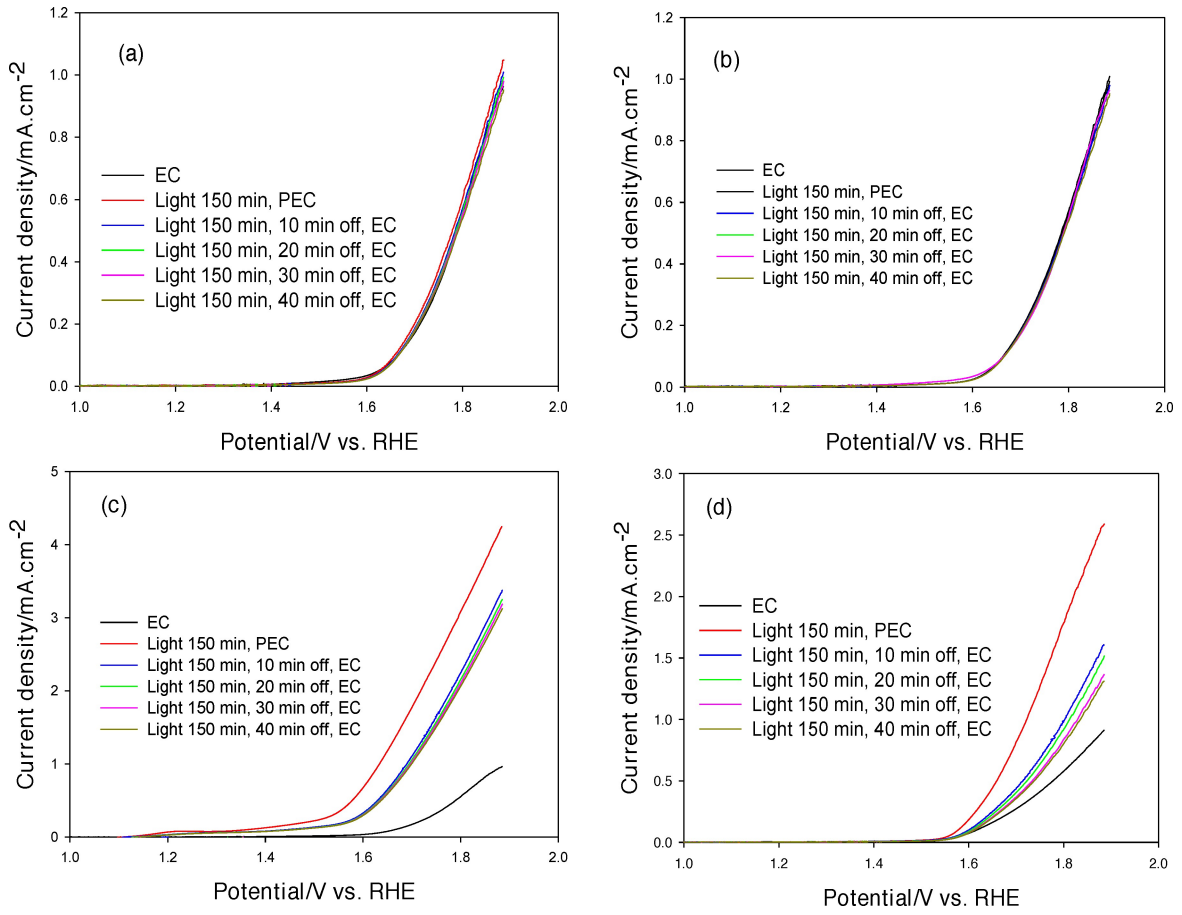

Figure 11. Light ON-OFF LSVs of (a) CTO-400, (b) CTO-700, (c) CTO-900 and (d) CTO-1100 (conditions: a scan rate of 10 mV.s^{-1}, at 25 °C and 1600 rpm in oxygen-purged 0.1 mol.dm^{-3} KOH electrolyte, under UV irradiation).

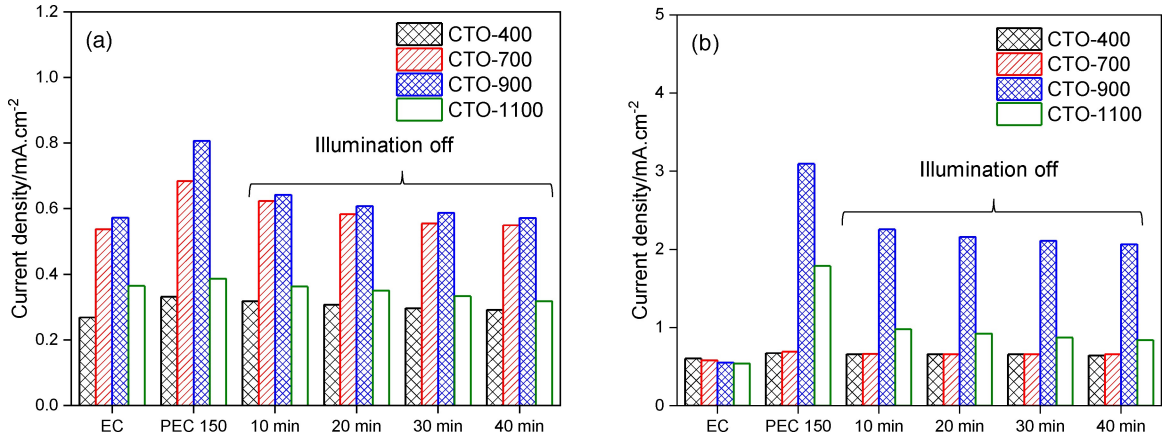

Figure 12. Current density vs. Light ON/OFF time plots for all the photo-electrocatalyst at (a) 0 rpm, and (b) 1600 rpm, at 1.8 V *vs.* RHE, in oxygen-purged 0.1 mol.dm^{-3} KOH electrolyte at 25 °C.

oversimplification of an intricate mechanism as it does not explain the large increase in PEC current at 150 minutes compared to the EC current (see Figure 12b). It is, however, to be expected that these reactions all occur at different rates with photo-induced charge separation being the fastest reaction followed by the OER (both potential bias and hole driven), and intercalation being the slowest reaction. This would mean that a large quantity of photo-excited electrons will reach the external circuit before being stabilised by potassium ions through intercalation. The increase in PEC current at 150 minutes is therefore due to the sum of (i) regular CTO surface OER, with the CTO surface being under a positive potential bias, (ii) hole driven OER, and (iii) non-stabilised photo-induced excited electrons reaching the external circuit.

Subsequent to the termination of illumination, but still under an applied potential bias, the OER is still driven (according to reaction 11) with the electrocatalyst now consisting of a combination of Co_3TeO_6 and $K_4Co_3TeO_6$, producing an oxidative current. In addition, the formed $K_4Co_3TeO_6$ is now also oxidised according to reaction 16, and thereby *discharging* to release additional electrons and thereby contributing to the current. The current density subsequent to the termination of illumination (see Figures 12a and 12b) is therefore due to the sum of the positive potential bias CTO surface OER (reaction 11) and electrons released as a result of de-intercalation (reaction 16), and it is therefore greater than under pure electrocatalytic conditions (see reaction 17, which is the sum of reactions 11 and 16). As this discharging process progresses, the total current (reactions 11 and 16) will decrease with time until the system is once more producing current only according to reaction 11. The enhanced dark current is therefore postulated to be a result of photo-induced charge storage (a *photocharging* process), through intercalation of an alkali metal ion (reactions 14 and 15), that serves to stabilise the photo-excited electrons, followed by a post-illuminated oxidative *discharging* process (reaction 15).

$$K_4Co_3TeO_6(+PB) \rightarrow Co_3TeO_6(+PB) + 4\,K^+ + 4e^- \quad (16)$$

$$K_4Co_3TeO_6(+PB) + 4OH^- \xrightarrow{dark} Co_3TeO_6(+PB) + 4\,K^+ + O_2 + 2H_2O + 8e^- \quad (17)$$

This postulated mechanism of the photo-induced intercalation of potassium ions (K^+) was corroborated by energy dispersive x-ray spectroscopy (EDX). As a baseline, EDX was conducted on a pure CTO-900 sample that was not produced into an ink, not soaked in KOH electrolyte, and not illuminated. From Figure S5 it is clear that the sample only consists of Co, Te and O. Subsequently, a CTO-900 sample was soaked in KOH electrolyte for 150 minutes in the absence of any illumination. This was done in duplicate and from Figure S6(a) and (b) it is clear that no potassium was taken up into the cobalt tellurium oxide structure. Finally, a CTO-900 sample was soaked in KOH electrolyte whilst being illuminated for 150 minutes. This was again done in duplicate and from Figure S7 (a) and (b) it is clear that potassium was indeed taken up into the cobalt tellurium oxide structure. All soaked samples were sequentially washed with deionised water, methanol, ethanol, and propanol, whilst being ultrasonicated, to clean the samples of any surface-bound electrolyte. The samples in Figures S6 and S7 also exhibit the presence of C, F and S. This originates from the Nafion that was used as a binder in producing the ink. It is clear that the photo-induced intercalation of potassium ions into the cobalt tellurium oxide structure, stabilising the photo-excited electrons, does indeed occur. Reactions 11–13 are therefore, in all likelihood, a true reflection of the mechanism at play describing the observed phenomenon of charge/energy storage, resulting not only in an enhanced PEC current after 150 min of illumination but also in sustained dark current subsequent to the termination of illumination.

Having shown that charge storage is the result of the photo-induced intercalation of potassium ions, it is furthermore essential to ascribe this observed phenomenon to, hopefully, a single compound given the fact that all the CTO samples (as per Table 3), apart from containing cobalt(II) tellurium oxide (Co_3TeO_6), also contains a substantial amount of cobalt oxide (CoO). To do this, pure CoO (Thermo Scientific, CAS: 1307-96-6) was prepared into an ink and subjected to the same electro-

catalytic and photo-electrocatalytic experiments. Linear sweep voltammograms (at 0 rpm and 1600 rpm) at different illumination times (0–150 minutes) and different post-illumination times (10–40 minutes), show that CoO is a better electrocatalyst and photo-electrocatalyst than Co_3TeO_6 as much greater current densities were obtained for the OER (Figures S8 and S9). However, CoO does not exhibit any charge storage capability as the current densities subsequent to the termination of illumination (10–40 minutes) are lower than the pure electrocatalytic (EC) sweeps in the absence of any illumination (Figure S10). The charge storage capability, via the intercalation of potassium ions, can therefore be solely ascribed to Co_3TeO_6.

The observed photo-induced charge storage process was further investigated employing a sequential switching experiment in the presence of a sodium metal ion. To do this a chronoamperometric (CA) experiment was conducted at 1 V (*vs.* Pt) in N_2-purged 0.1 mol.dm^{-3} Na_2SO_4 at 25 °C, with the termination of UV-light every 10 min (Figure 13). After an initial induction period of 10 min, the current density quickly increases and then stabilises over a period of in excess of 150 min. Sequential on-off switching did not result in an immediate drop in current back to the baseline, which already attests to the charge storage capacity of the material. Upon the permanent termination of illumination, an initial decrease in current is observed, where after the decay in current is inhibited, which points to a slow discharge of the material. This work has shown that, as a photo-electrocatalyst, cobalt(II) tellurium oxide (Co_3TeO_6) facilitates solar to chemical energy conversion, storage and subsequent energy release. Photo-induced charge separation led to charge storage through intercalation, whereafter the charge, upon the termination of illumination, is slowly released in the dark resulting in a prolonged OER. Under these conditions, higher efficiency water splitting, compared to pure electrocatalytic (EC) water splitting, can not only be attained during daylight hours but can also be continued in the dark. This class of materials, i.e. metal tellurium oxides, would therefore seem to lend itself to renewable energy conversion, storage and subsequent energy usage. This is in line with our earlier work whereby europium(III) tellurium oxide[35] and nickel(II) tellurium oxide[7,71] exhibit similar results.

3. Conclusions

Cobalt(II) tellurium oxide was synthesised *via* the sol gel synthetic approach and calcined at 400 °C (CTO-400), 700 °C (CTO-700), 900 °C (CTO-900) and 1100 °C (CTO-1100). These nanomaterials were physically characterized and their electrochemical (EC) and photo-electrochemical (PEC) performance towards the OER was evaluated in alkaline media. The surface morphology of low calcined nanomaterials exhibited irregular-shaped materials with high agglomeration of particles that overlay one another. Hexagonal-shaped nanomaterials were formed as the calcination temperature was increased demonstrating less agglomeration. The purity of these materials was confirmed employing both EDX and XRD, while the stoichiometric composition was established as being Co_3TeO_6, with increasing crystallinity having been observed as the calcination temperature was increased.

Under PEC conditions both CTO-400 and CTO-700 do not experience any significant increase in OER activity, compared to the non-illuminated EC condition, whereas CTO-900 sees the greatest increase in activity followed by CTO-1100 to a much lesser extent. At lower calcining temperatures the samples prove to be much more amorphous with crystallinity increasing as the calcining temperature increases. This high PEC activity for CTO-900 would seem to be a direct result of the sample consisting predominantly of Co_3TeO_6, whereas the CTO-1100 sample would seem to be covered with a layer of Co_3O_4 and thereby rendering it not as active. High crystallinity therefore does not necessarily result in high PEC activity. It has furthermore been observed that the PEC activity increases with increased illumination time, which is coupled with an associated exponential decrease in the charge transfer resistance and a

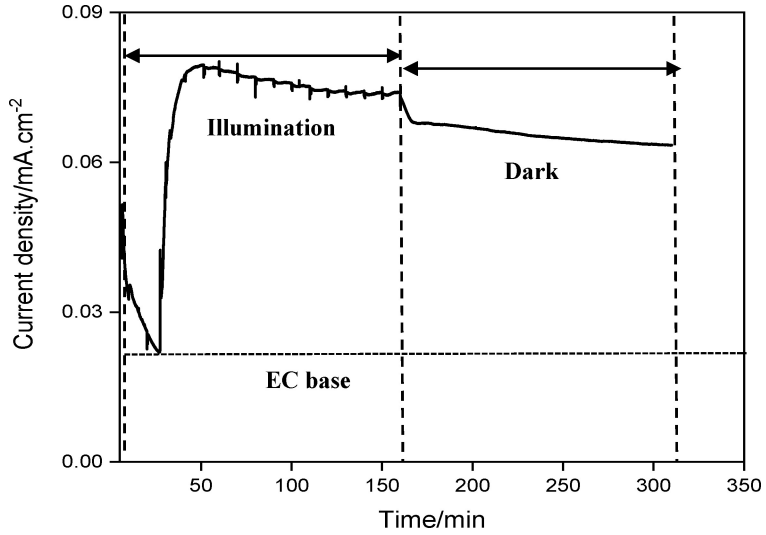

Figure 13. Sequential light switching CA plot for CTO-900 at 1 V (*vs.* Pt) in N_2-purged 0.1 mol.dm^{-3} Na_2SO_4 solution at 25 °C.

linear increase in the charge transfer rate constant. Not only does the CTO-900 sample exhibit the highest PEC activity, but it also exhibits the highest photo-induced charge storage capacity (through intercalation of potassium ions into the Co_3TeO_6 structure) that allows for subsequent dark current release (in excess of 40 min). Subsequent to an illumination time of 150 min the CTO-900 sample displayed much higher EC OER activity (3.6 times) in the dark (40 min after light termination) compared to the non-illuminated EC OER activity, i.e. 2.07 mA cm^{-2} compared to 0.58 mA cm^{-2}. In this regard this class of materials, i.e. metal tellurium oxides, exhibits huge promise in bringing about solar to chemical energy conversion and storage, together with subsequent energy release and usage.

Acknowledgements

The authors wish to express their appreciation to the North-West University, Potchefstroom, South Africa and the National Research Foundation (NRF) of South Africa (Grant No. 120754, 85364, 90698, 93205, 119314) for research facilities, funding and postdoctoral fellowships awarded to OA Oyetade and NH Zingwe. This research was also partially supported by the Faculty of Science and the University Research Council of the University of Johannesburg, Johannesburg, South Africa.

Conflict of Interests

There are no conflicts of interest to declare.

Data Availability Statement

The data that support the findings of this study are available from the corresponding author upon reasonable request.

Keywords: cobalt(II) tellurium oxide · photo-electrocatalyst · oxygen evolution reaction · intercalation · dark current

[1] A. Fujishima, K. Honda, *Nature* **1972**, *238*, 37–38.
[2] S. Cao, C. J. Wang, W. F. Fu, Y. Chen, *ChemSusChem.* **2017**, *10*, 4306–4323.
[3] T. Mohammadi, Y. Ghayeb, T. Sharifi, M. M. Momeni, *New J. Chem.* **2020**, *44*, 2339–2349.
[4] Q. Zeng, J. Bai, J. Li, L. Xia, K. Huang, X. Li, B. Zhou, *J. Mater. Chem. A* **2015**, *3*, 4345–4353.
[5] Q. Zeng, J. Li, L. Li, J. Bai, L. Xia, B. Zhou, *Appl. Catal. B* **2017**, *217*, 21–29.
[6] O. A. Oyetade, R. J. Kriek, *Electrocatalysis* **2019**, *11*, 35–45.
[7] M. Z. Iqbal, E. Carleschi, B. P. Doyle, R. J. Kriek, *ACS Appl. Energ. Mater.* **2019**, *2*, 8125–8137.
[8] C. Ding, J. Shi, Z. Wang, C. Li, *ACS Catal.* **2016**, *7*, 675–688.
[9] W. D. Chemelewski, H.-C. Lee, J.-F. Lin, A. J. Bard, C. B. Mullins, *J. Am. Chem. Soc.* **2014**, *136*, 2843–2850.
[10] M. Z. Iqbal, R. J. Kriek, *Electrocatalysis* **2018**, *9*, 279–286.
[11] B. Zhang, X. Zheng, O. Voznyy, R. Comin, M. Bajdich, M. García-Melchor, L. Han, J. Xu, M. Liu, L. Zheng, *Science* **2016**, *352*, 333–337.
[12] M. Gao, W. Sheng, Z. Zhuang, Q. Fang, S. Gu, J. Jiang, Y. Yan, *J. Am. Chem. Soc.* **2014**, *136*, 7077–7084.
[13] M. Huynh, D. K. Bediako, D. G. Nocera, *J. Am. Chem. Soc.* **2014**, *136*, 6002–6010.
[14] B. Sidhureddy, J. S. Dondapati, A. Chen, *Chem. Commun.* **2019**, *55*, 3626–3629.
[15] B. Chen, M. Humayun, Y. Li, H. Zhang, H. Sun, Y. Wu, C. Wang, *ACS Sustainable Chem. Eng.* **2021**, *9* (42), 14180–14192.
[16] Y. Liu, H. Wang, D. Lin, C. Liu, P.-C. Hsu, W. Liu, W. Chen, Y. Cui, *Energy Environ. Sci.* **2015**, *8*, 1719–1724.
[17] L.-A. Stern, L. Feng, F. Song, X. Hu, *Energy Environ. Sci.* **2015**, *8*, 2347–2351.
[18] M. Qin, L. Chen, H. Zhang, M. Humayun, Y. Fu, X. Xu, X. Xue, C. Wang, *Chem. Eng. J.* **2023**, *454* (2),140230.
[19] C. B. Njoku, R. J. Kriek, *Electrocatalysis* **2018**, *10*, 305–313.
[20] J. G. Lee, J. Hwang, H. J. Hwang, O. S. Jeon, J. Jang, O. Kwon, Y. Lee, B. Han, Y.-G. Shul, *J. Am. Chem. Soc.* **2016**, *138*, 3541–3547.
[21] H. Sun, L. Li, M. Humayun, H. Zhang, Y. Bo, X. Ao, X. Xu, K. Chen, K. Ostrikov, K. Huo, W. Zhang, C. Wang, Y. Xiong, *Appl. Catal. B* **2022**, *305*, 121088.
[22] G. L. Tian, M. Q. Zhao, D. Yu, X. Y. Kong, J. Q. Huang, Q. Zhang, F. Wei, *Small* **2014**, *10*, 2251–2259.
[23] H. W. Park, D. U. Lee, L. F. Nazar, Z. Chen, *J. Electrochem. Soc.* **2013**, *160*, A344–A350.
[24] G. Hodes, D. Cahen, J. Manassen, *Nature* **1976**, *260*, 312–313.
[25] S. R. Pendlebury, A. J. Cowan, M. Barroso, K. Sivula, J. Ye, M. Grätzel, D. R. Klug, J. Tang, J. R. Durrant, *Energy Environ. Sci.* **2012**, *5*, 6304–6312.
[26] N. Kiama, C. Ponchio, *Surf. Coat. Technol.* **2020**, *383*, 125257.
[27] Y.-H. Chiu, K.-D. Chang, Y.-J. Hsu, *J. Mater. Chem. A* **2018**, *6*, 4286–4296.
[28] N. T. Hahn, C. B. Mullins, *Chem. Mater.* **2010**, *22*, 6474–6482.
[29] Y. Fu, C.-L. Dong, W. Zhou, Y.-R. Lu, Y.-C. Huang, Y. Liu, P. Guo, L. Zhao, W.-C. Chou, S. Shen, *Appl. Catal. B* **2020**, *260*, 118206.
[30] C. Ding, J. Shi, D. Wang, Z. Wang, N. Wang, G. Liu, F. Xiong, C. Li, *Phys. Chem. Chem. Phys.* **2013**, *15*, 4589–4595.
[31] D. K. Zhong, D. R. Gamelin, *J. Am. Chem. Soc.* **2010**, *132*, 4202–4207.
[32] T. Tatsuma, S. Saitoh, Y. Ohko, A. Fujishima, *Chem. Mater.* **2001**, *13*, 2838–2842.
[33] S. N. Lou, Y. H. Ng, C. Ng, J. Scott, R. Amal, *ChemSusChem.* **2014**, *7*, 1934–1941.
[34] S. N. Lou, N. Yap, J. Scott, R. Amal, Y. H. Ng, *Sci. Rep.* **2014**, *4*, 7428.
[35] R. J. Kriek, M. Z. Iqbal, B. P. Doyle, E. Carleschi, *ACS Appl. Energ. Mater.* **2019**, *2*, 4205–4214.
[36] W. Shi, F. Guo, M. Li, Y. Shi, M. Shi, C. Yan, *Appl. Surf. Sci.* **2019**, *473*, 928–933.
[37] S. Moridon, M. Salehmin, M. Mohamed, K. Arifin, L. Minggu, M. Kassim, *Int. J. Hydrogen Energy* **2019**, *44* (47), 25495–25504.
[38] S. Xiao, Y. Liu, X. Wu, L. Gan, H. Lin, L. Zheng, S. Dai, P. Liu, H. Yang, *J. Mater. Chem. A* **2021**, *9*, 14786–14792.
[39] S. Wang, L. Zhao, W. Huang, H. Zhao, J. Chen, Q. Cai, X. Jiang, C. Lu, W. Shi, *Mater. Res. Bull.* **2021**, *135*, 111161.
[40] X. Yang, W. Chen, Y. Liu, B. Liang, J. Hu, H. Huang, *J. Alloys and Compd.* **2023**, *939*, 168807.
[41] N. Wang, X. Li, *Inorg. Chem. Commun.* **2018**, *92*, 14–17.
[42] Y. Ouyang, Q. Yang, *J. Colloid Interface Sci.* **2023**, *644*, 346–357.
[43] T. Chen, C. Yang, S. Rajendran, M. Sawangphruk, X. Zhang, J. Qin, *Fuel* **2023**, *331*, 125594.
[44] F. Guo, W. Shi, C. Zhu, H. Li, Z. Kang, O. Co, *Appl. Catal. B* **2018**, *226*, 412–420.
[45] K. P. D. Savio, J. Fletcher, K. Smith, R. Iyer, J. M. Bao, F. C. Robles Hernández, *Appl. Catal. B* **2016**, *182*, 449–455.
[46] C. Lu, D. Yang, L. Wang, S. Wen, D. Cao, C. Tu, L. Gao, Y. Li, Y. Zhou, W. Huang, *J. Alloys and Compd.* **2022**, *904*, 164046.
[47] N. P. Rini, N. I. Istiqomah, M. S. Sunarta, E. Suharyadi, *Case Stud. Chem. Environ. Eng.* **2023**, *7*, 100301.
[48] X. Liu, Q. Li, Y. Fan, W. Chen, L. Lin, W. Xu, H. Zhuang, Q. Li, *Mater. Lett.* **2022**, *315*, 132010.
[49] N.-I. Kim, Y. J. Sa, S.-H. Cho, I. So, K. Kwon, S. H. Joo, J.-Y. Park, *J. Electrochem. Soc.* **2016**, *163*, F3020.
[50] M. Takumi, T. Masamitsu, K. Nagata, *J. Phys. Condens. Matter.* **2002**, *14*, 10609–10613.
[51] T. Ito, H. Sawada, *Zeitschrift fuer Kristallographie, Kristallgeometrie, Kristallphysik, Kristallchemie* **1940**, *102*, 13–25.
[52] O. Lindqvist, W. Mark, J. Moret, *Acta Cryst. B* **1975**, *31*, 1255–1259.
[53] M. J. Redman, E. G. Steward, *Nature (London)* **1962**, *193*, 867.
[54] N. C. Tombs, H. P Rooksby, *Nature (London)* **1950**, *165*, 442–443.
[55] J. Isasi, *J. Alloys and Compd.* **2001**, *322*, 89–96.
[56] X. Liu, T. C. Prewitt, *Phys Chem Minerals* **1990**, *17*, 168–172.

[57] R. Becker, M. Johnsson, H. Berger, *Acta Crystallogr. Sect. C* **2006**, *62*, 67–69.
[58] M. K. Uddin, U. Baig, *J. Cleaner Prod.* **2019**, *211*, 1141–1153.
[59] L. Zhong, Y. Bao, L. Feng, *Electrochim. Acta* **2019**, *321*, 134656.
[60] K. Wang, Z. Ye, C. Liu, D. Xi, C. Zhou, Z. Shi, H. Xia, G. Liu, G. Qiao, *ACS Appl. Mater. Interfaces* **2016**, *8*, 2910–2916.
[61] P. Mohanty, A. R. E. Prinsloo, B. P. Doyle, E. Carleschi, C. J. Sheppard, *AIP Adv.* **2018**, *8*, 056424.
[62] Z. Liu, T. Duchoň, H. Wang, D. C. Grinter, I. Waluyo, J. Zhou, Q. Liu, B. Jeong, E. J. Crumlin, V. Matolín, *Phys. Chem. Chem. Phys.* **2016**, *18*, 16621–16628.
[63] L. Zhong, Y. Bao, L. Feng, *Electrochim. Acta* **2019**, *321*, 134656.
[64] J. A. McLeod, A. Buling, R. J. Green, T. D. Boyko, N. A. Skorikov, E. Z. Kurmaev, M. Neumann, L. D. Finkelstein, N. Ni, A. Thaler, *J. Phys. Condens. Matter* **2012**, *24*, 215501.
[65] J.-W. Kim, S. J. Lee, P. Biswas, T. I. Lee, J.-M. Myoung, *Appl. Surf. Sci.* **2017**, *406*, 192–198.
[66] N. Bingwa, S. Bewana, M. J. Ndolomingo, N. Mawila, B. Mogudi, P. Ncube, E. Carleschi, B. P. Doyle, M. Haumann, R. Meijboom, *Appl. Catal. A* **2018**, *555*, 189–195.
[67] V. Maruthapandian, M. Mathankumar, V. Saraswathy, B. Subramanian, S. Muralidharan, *ACS Appl. Mater. Interfaces* **2017**, *9*, 13132–13141.
[68] J. Rossmeisl, Z.-W. Qu, H. Zhu, G.-J. Kroes, J. K. Nørskov, *J. Electroanal. Chem.* **2007**, *607*, 83–89.
[69] L. Gong, D. Ren, Y. Deng, B. S. Yeo, *ACS Appl. Mater. Interfaces* **2016**, *8*, 15985–15990.
[70] M. S. Khan, M. N. Ashiq, M. F. Ehsan, T. He, S. Ijaz, *Appl. Catal. A* **2014**, *487*, 202–209.
[71] M. Z. Iqbal, E. Carleschi, B. P. Doyle, R. J. Kriek, *Phys. Status Solidi A* **2023**, *220*, 2300002.
[72] A. Zia, S. Hamid, M. F. Ehsan, *J. Mater. Sci. Mater. Electron.* **2018**, *29*, 20271–20279.
[73] L. Xu, C. Qin, H. Xie, Y. Huang, L. Qin, H. J. Seo, *Mater. Lett.* **2016**, *184*, 1–4.
[74] S. Hernández, D. Hidalgo, A. Sacco, A. Chiodoni, A. Lamberti, V. Cauda, E. Tresso, G. Saracco, *Phys. Chem. Chem. Phys.* **2015**, *17*, 7775–7786.
[75] S. Xie, W. Wei, S. Huang, M. Li, P. Fang, X. Lu, Y. Tong, *J. Power Sources* **2015**, *297*, 9–15.
[76] G. M. Kanyolo, T. Masese, N. Matsubara, C.-Y. Chen, J. Rizell, Z.-D. Huang, *Chem. Soc. Rev.* **2021**, *50*, 3990–4030.

Manuscript received: January 15, 2024
Revised manuscript received: May 30, 2024
Version of record online: August 30, 2024